1 **Evaluation of filtering methods for use on high-frequency measurements of**

2 **landslide displacements**

3 Sohrab Sharifi[1], Michael T. Hendry[1], Renato Macciotta[1], Trevor Evans[2]

4 *[1]Department of Civil and Environmental Engineering, University of Alberta, Edmonton, AB,*
5 *Canada*

6 *[2]Canadian National Railway, Kamloops, BC, Canada*

8 **Abstract**

9 Displacement monitoring is a critical control for risks associated with potentially sudden slope

10 failures. Instrument measurements are, however, obscured by the presence of scatter. Data

11 filtering methods aim to reduce the scatter and therefore enhance the performance of early

12 warning systems (EWSs). The effectiveness of EWSs depends on the lag time between the onset

13 of acceleration and its detection by the monitoring system, such that a timely warning is issued

14 for implementation of consequence mitigation strategies. This paper evaluates the performance

15 of three filtering methods (simple moving average, Gaussian-weighted moving average, and

16 Savitzky-Golay), and considers their comparative advantages and disadvantages. The evaluation

17 utilized six levels of randomly generated scatter on synthetic data as well as high-frequency global

18 navigation satellite system (GNSS) displacement measurements at the Ten-mile landslide in

19 British Columbia, Canada. The simple moving average method exhibited significant

20 disadvantages compared to the Gaussian-weighted moving average and Savitzky-Golay

21 approaches. This paper presents a framework to evaluate the adequacy of different algorithms

22 for minimizing monitoring data scatter.

23 **Keywords:** Landslide; Early Warning System; Scatter; Filter; Gaussian-Weighted Moving

24 Average, Savitzky-Golay

1. Introduction

Landslides are associated with significant losses in terms of mortality and financial consequences in countries all over the world. In Canada, landslides have cost Canadians approximately \$10 billion since 1841 (Guthrie, 2013) and more than \$200 million annually (Clague and Bobrowsky, 2010). Essential infrastructure, such as railways and roads that play vital roles in the Canadian economy, can be exposed to damage if it transverses landslide-prone areas. Attempting to completely prevent landslides is typically infeasible, as stabilizing options and realignment may be cost-prohibitive or lead to environmental damage. This accentuates the significance of adopting strategies that require constant monitoring to mitigate the consequences of sudden landslide collapses (Vaziri et al., 2010; Macciotta and Hendry, 2021).

In recent years, detailed studies have addressed the use of early warning systems (EWSs) as a robust approach to landslide risk management (Intrieri et al., 2012; Thiebes et al., 2014; Atzeni et al., 2015; Hongtao, 2020). The United Nations defines an EWS as "a chain of capacities to provide adequate warning of imminent failure, such that the community and authorities can act accordingly to minimize the consequences associated with failure" (UNISDR, 2009). Although an EWS comprises various components acting interactively, the core of its performance relies on its ability to detect the magnitude and rate of landslide displacement (Intrieri et al., 2012). Given that the timely response of an EWS determines its effectiveness, an accurate sense of landslide velocity and acceleration is necessary. Monitoring instruments able to provide real-time or near real-time readings such as global navigation satellite systems (GNSSs) and some remote sensing techniques are, satisfactory for this purpose (Yin et al., 2010; Tofani et al., 2013; Benoit et al., 2015; Macciotta et al., 2016; Casagli et al., 2017; Chae et al., 2017; Rodriguez et al., 2017, 2018, 2020; Huntley et al., 2017; Intrieri et al., 2018; Journault et al., 2018; Carlà et al., 2019; Deane, 2020; Woods et al., 2020, 2021). These instruments can record the displacement of locations at the surface of the landslide with high temporal resolution, which allows the monitoring system to track movements on the order of a few millimeters per year. In practice, the results are usually

52 obscured by the presence of scatter, also known as noise, and outliers that affect the quality of

53 observations. These unfavorable interferences do not reflect the true behavior of the ground

54 motion and stem from sources such as the external environment and the quality of the

55 communication signals and wave propagation in the case of remote sensing techniques (Wang,

56 2011; Carlà et al., 2017b).

57 Scatter can be defined as measurement data that are distributed around the "true" displacement

58 trend, such that the average difference between the scatter and the displacement trend is zero

59 and has a finite standard deviation. Scatter in displacement measurements can significantly

60 impact the evaluation of slope movements performed on unfiltered data and decrease the

61 reliability of an EWS. This can lead to false warnings of slope acceleration or unacceptable time

62 lags between the onset of slope failure and its identification, and therefore a loss of credibility for

63 an EWS (Lacasse and Nadim, 2009). As a result, scatter should be reduced as much as possible

64 without removing the true slope displacement trends. The application of algorithms that work as

65 filters aims to minimize the amplitude of measured scatter around the displacement trend.

66 Several approaches have been proposed to filter displacement measurements based on either

67 the frequency or time domain. Fourier and wavelet transformations aim to find the frequency

68 characteristics of the data, then attenuate or amplify certain frequencies. These approaches are

69 discussed in Karl (1989), who suggests they are generally unsuitable for non-stationary data such

70 as monitoring data time series. Filters that work on the time domain can be classified as recursive,

71 kernel, or regression filters. Recursive filters, such as the exponential filtering function, calculate

72 the filtered value at a given time based on the previous filtered value. Kernel filters, which include

73 simple moving average (SMA) and Gaussian-weighted moving average (GWMA), calculate the

74 filtered values as the weighted average of neighbouring measurements. Of these two kernel

75 filters, SMA is frequently used in the literature largely due to its simplicity (Dick et al., 2015;

76 Macciotta et al., 2016, 2017b; Carlà et al., 2017a,b, 2018, 2019; Bozzano et al., 2018; Intrieri et

77 al., 2018; Kothari and Momayez, 2018; Chen and Jiang, 2020; Zhou et al., 2020; Deng et al.,

78 2021; Desrues et al., 2021; Grebby et al., 2021; Zhang et al., 2021a,b). Regression filters

79 calculate the filtered values by means of regression analysis on unfiltered values (e.g., Savitzky-

80 Golay, or S-G) (Savitzky and Golay, 1964; William, 1979; Cleveland, 1981; Cleveland and Devlin,

81 1988; Reid et al., 2021). Carlà et al., (2017b) studied both SMA and exponential filtering on

82 multiple failed landslide cases and concluded the latter is inferior in terms of accuracy of failure

83 time prediction. On the other hand, Carri et al. (2021) cautioned the designers and users of EWSs

84 against the use of SMA when rapid movements are expected. However, published applications

85 of filters other than SMA for landslide monitoring are scarce, and studies dedicated to comparing

86 the functionality of other filters to that of SMA are limited.

87 This paper presents an approach to detect and remove outliers, evaluates the performance of

88 three filters (SMA, GWMA, and S-G), and assesses their suitability to be utilized in an EWS. We

89 evaluated three filters against the following criteria: 1) scatter is minimized, 2) true underlying

90 displacement trends are kept with as little modification as possible, and 3) filtered displacement

91 trends detect acceleration episodes in a timely manner. Moreover, the paper investigates the

92 significance of the time lag between a landslide acceleration event and its identification by a

93 monitoring system for the three filters evaluated.

94 **2. Methodology**

95 **2.1. Synthetic Data Generation**

96 A numerical analysis on a synthetic dataset approach was adopted, which consists of synthetic

97 dataset scenarios generated to resemble typical landslide displacement measurements, including

98 acceleration and deceleration periods. These scenarios are idealizations based on observations

99 of typical landslide displacements published in the literature (Leroueil, 2001; Intrieri et al., 2012;

100 Macciotta et al., 2016; Schafer, 2016; Carlà et al., 2017a; Scoppettuolo et al., 2020). A total of 12

101 dimensionless scenarios were built, with all data between the coordinates $x=0$, $y=0$ and $x=1$, $y=1$.

102 The x value represents time, and normalization between 0 and 1 allows for extrapolation of the

103   findings for variable displacement measurement frequencies (e.g., the full range of x could

104   represent a week, a month, a year). The analysis of synthetic data focuses on the ability of

105   different algorithms to minimize scatter and identify changes in measured trends; therefore, y

106   represents any of the displacement measurement metrics of interest, e.g., displacement,

107   cumulative displacement, velocity, inverse velocity, etc. Mathematical equations and graphical

108   illustrations of the 12 scenarios are shown in Fig. 1.

109   Nine of the scenarios are referred to as harmonic scenarios, which are characterized by gradual

110   changes in the trend of parameter $y.$ The remaining three scenarios show sudden variations at or

111   near x=0.5, and are referred to as instantaneous scenarios. Considering the discrete nature of

112   instrument measurements, and to account for different ranges in measurement frequencies, each

113   scenario was generated several times, each time with a different number of points (Table 1).
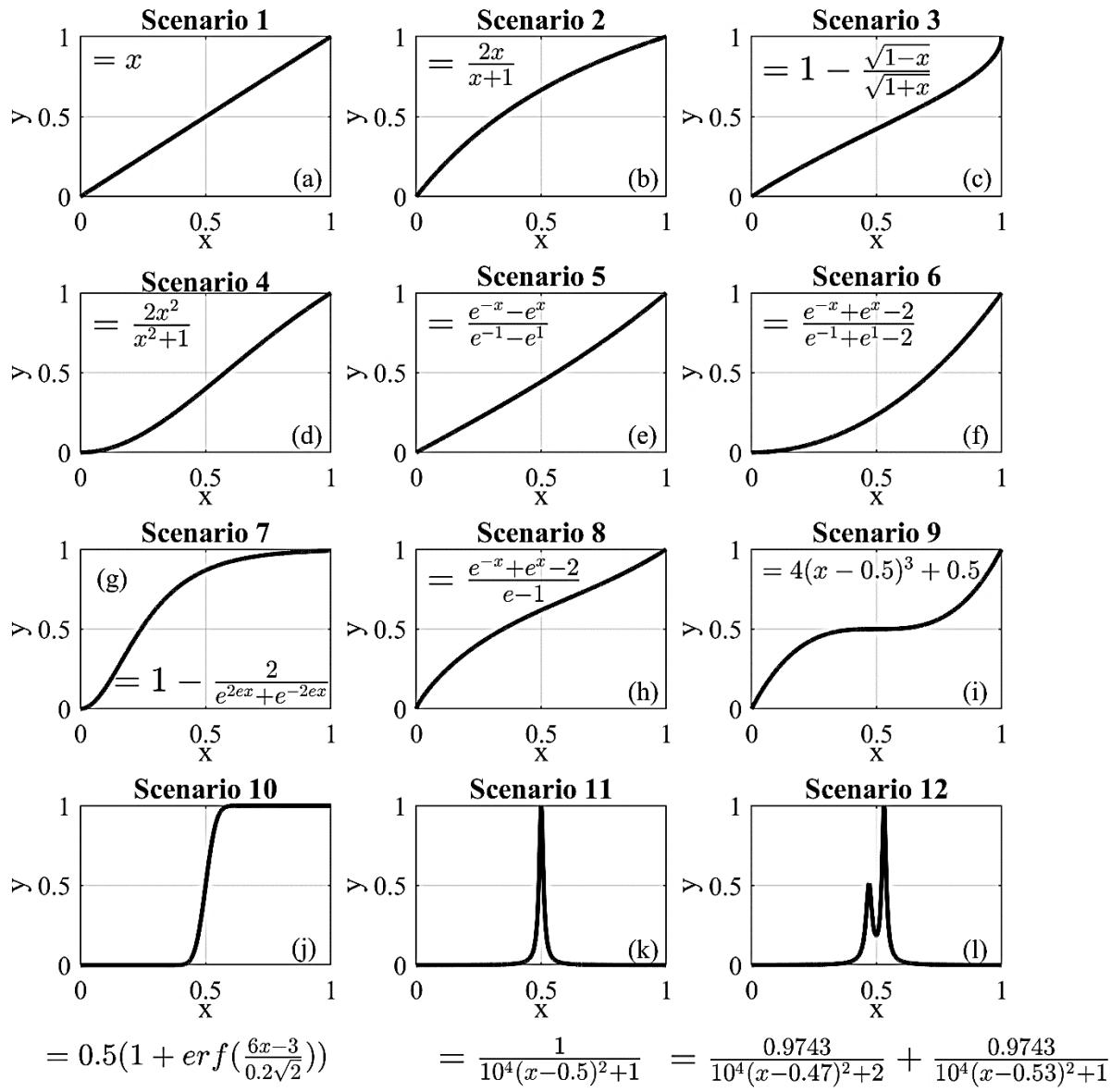
Fig. 1 *Configuration of all synthetically generated scenarios*

Table 1 *Number of points used to generate scenarios and examples of their corresponding time spans represented by the range of x from 0 to 1 if the measurement frequency is known (1-h and 1-m readings for illustrative purposes).*

Number of points	Example monitoring frequency			
	1-h readings		1-m readings	
1000	41.7	Days	16.7	Hours
3000	4.1	Months	2.1	Days
9000	1.0	Years	6.3	Days

20000	2.3	Years	2.0	Weeks
40000	4.6	Years	4.0	Weeks
86000	9.8	Years	2.0	Months
250000			5.8	Months
500000			0.9	Year
750000			1.4	Years
1.00E+6			1.9	Years

120

121   The next step was adding random scatter to the scenarios to represent unfiltered displacement

122   measurements. Macciotta et al. (2016) show the scatter in displacement monitoring for a GNSS

123   used in their analyses fitted a Gaussian distribution. We validated the scatter distribution fit

124   approximates a Gausian distribution for the displacement data scatter of the case study in this

125   paper. This assumption, however, has an underpinning theoretical base established by the central

126   limit theorem in probability theory. It states that mathematical summation of independent variables

127   (such as scatter) goes toward a Gaussian distribution (Smith, 2013). As a result, the scatter was

128   randomly produced from a normal distribution centred at zero, with extreme values truncated

129   between −1 and 1 and a standard deviation of 0.20. Random generation of the scatter followed

130   the techniques outlined in Clifford (1994) known as the acceptance-rejection method, which

131   generates scatter values through a series of iterations until the algorithm generates the initial

132   normal distribution. The amplitude of the scatter around the trend in parameter y was defined for

133   each scenario by scaling the randomly generated scatter. This allowed for investigation of the

134   effect of different scatter magnitudes on the performance of the filters. Scaling was done by

135   defining the ratio $n/t,$ which is the ratio of scatter amplitude (maximum deviation around the trend,

136   termed n) to the range of values of the trend (t) in each scenario. Six levels of n/t (0.001, 0.005,

137   0.010, 0.050, 0.100, and 0.150) were considered when performing the analysis to cover a range

138   of possible levels of scatter in unfiltered measurements. Fig. 2 shows two samples of synthetic

139 unfiltered scenarios that are the result of superimposing scatter with *n/t* values of 0.05 and 0.10,

140 respectively, on scenario No. 7.
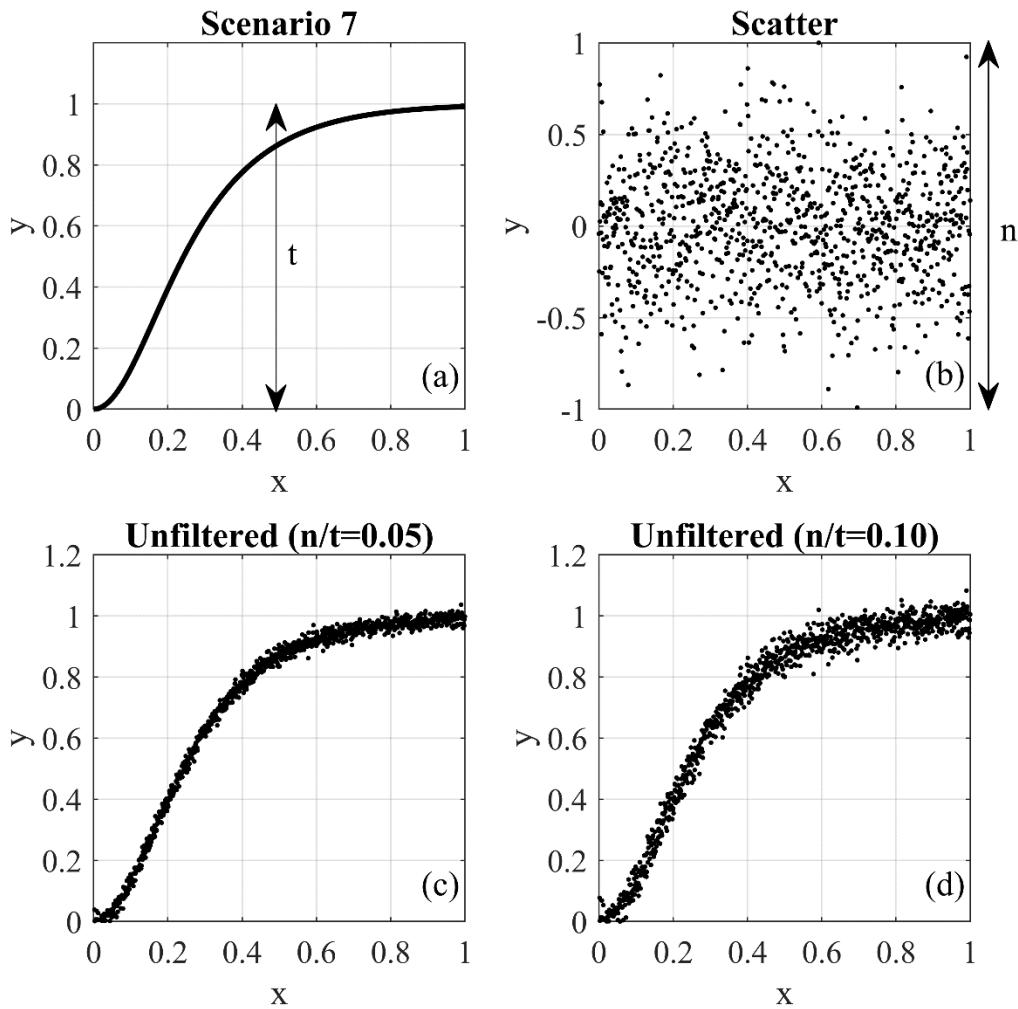
141

142 **Fig. 2** *The procedure of generating a scenario with scatter: (a) generated scenario trend, (b) randomly*
143   *generated scatter, and two scenarios with scatter based on n/t values of (c) 0.05 and (d) 0.10*

144 **2.2 Data Processing Approaches**

145 *2.2.1. Simple moving average*

146 SMA is a well-known method for scatter reduction that attempts to reduce scatter by calculating

147 the arithmetic mean of neighbouring points' values. A constant-length interval (window or

148 bandwidth) is used for the calculation for each point; this is also termed a "running" average.

149 Equation 1 is the formulation of this method, which was used by Macciotta et al. (2016) to analyze

150 GNSS data scatter:

151
$$\hat{y}_i = \frac{\sum_{i-\frac{p-1}{2}}^{i+\frac{p-1}{2}} y_j}{p} ,$$
(1)

152 where $\hat{y}_i$ is the filtered value, y_j is the unfiltered value, and p is the window length. The window

153 length is constant across the dataset except for regions near the boundaries where fewer points

154 are available. Accordingly, p will be adjusted to the number of available points that are indeed

155 less than the value set by the user. This will cause variation in the effectiveness of the method at

156 the extremes, which needs to be considered when evaluating the results of this approach.

157 *2.2.2. Gaussian-weighted moving average*

158 Varying the weights of the measurements within the calculation window in SMA can be used to

159 develop different filtering methods. The largest weight can be given to the measurement at the

160 time for which the calculation is being done, with weights decreasing for measurements farther

161 away in time. One simple weighting function that can be adopted is the Gaussian (normal)

162 distribution. Eq. 2 is the formulation of the Gaussian-weighted moving average (GWMA):

163
$$\hat{y}_i = \sum_{i-\frac{p-1}{2}}^{i+\frac{p-1}{2}} w_j y_j ,$$
(2)

164 where w_j is the weight coefficient based on the Gaussian distribution and the other terms follow

165 the same definition as per SMA.

166 *2.2.3. Savitkzy-Golay*

167 S-G fits a low-degree polynomial equation to the unfiltered measurements within a window and

168 defines the filtered measurements using the fitted curve (Schafer, 2011). Although this procedure

169 seems dissimilar from the weighted averaging as discussed for GWMA, its function can be

170 transformed into a kernel concept using the least-squares method if the data points are evenly

171 spaced. The detailed procedure is presented in Appendix A. Fig. 3 shows the weight kernel over

172 a window of seven points attained by fitting a quadratic polynomial. An immediate observation is

173   that some points are given negative weights. If points are not evenly spaced, the weighting kernel

174   cannot be used and a local regression analysis should be periodically conducted for each point.

175   Such filtering is known as locally estimated scatterplot smoothing (LOESS). This decreases the

176   computational efficiency of filter performance and exponentially increases the execution time.
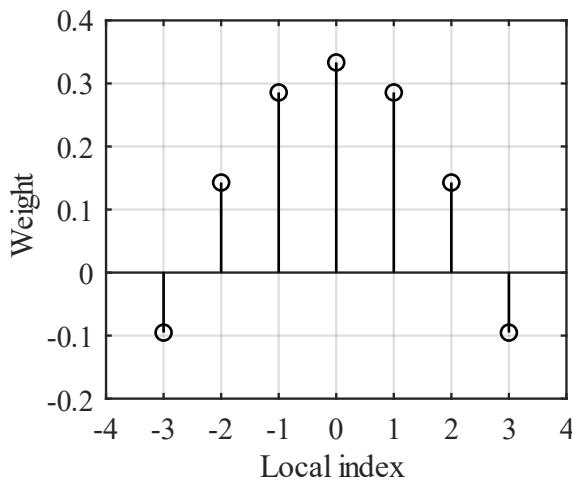
177

178   ***Fig. 3*** *The weighting kernel of the Savitzky-Golay filter for seven points*

179   **2.3 Evaluation of Processing Algorithms**

180   The synthetic monitoring data and data from the case studies were filtered using SMA, GWMA,

181   and S-G techniques. The filters were applied with different lengths of moving windows, from 0.01

182   (1%) to 0.1 (10%) of all monitoring points, referred to as the bandwidth ratio. These limits for the

183   bandwidth ratio were selected based on literature reports for SMA. In the filtration process, we

184   only used the points prior to the time for which the calculation is being made (point of interest,

185   Fig. 4). This is to reflect the reality of displacement monitoring information as applied to EWSs.

186   To this end, filters used the first half of their kernels, but the weights were multiplied by 2 in

187   comparison to a symmetric window in order to keep the sum of weights equal to 1.
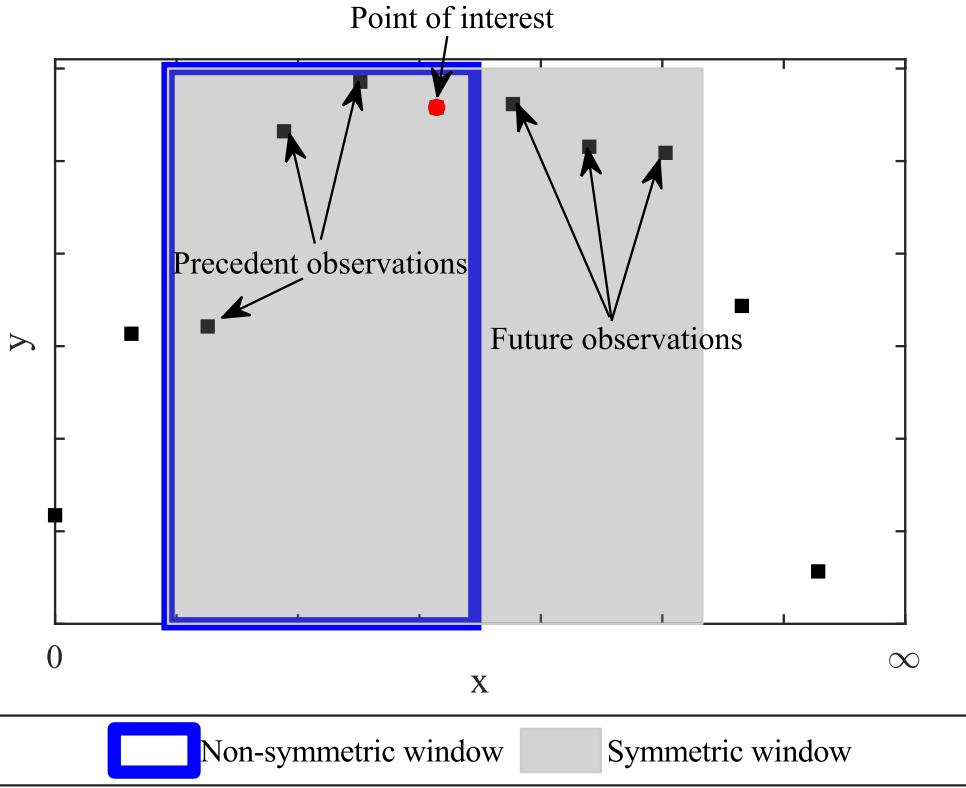
Fig. 4. Concept of symmetric and non-symmetric window types in the filtration process

All of these filters require the definition of a bandwidth. A roughness factor was defined to aid in

the evaluation of the effect of bandwidth in reducing scatter. This factor is defined as:

$$J_2 = \frac{\int (\hat{y}'')^2 \, dx}{R_a},$$ (3)

$$R_a = \int (y'')^2 \, dx,$$ (4)

where J_2 is the roughness factor, $\hat{y}''$ is the second derivative of filtered measurements, R_a is the

absolute roughness computed by Eq. 4, and y'' is the second derivative of unfiltered

measurements. The second derivative measures how much the slope of the line connecting two

consecutive points changes, which itself is an indication of fluctuation. The greater this second

derivative, the greater the variation. J_2 was normalized to the overall curvature of the unfiltered

scenario to determine the relative scatter reduction after the application of a filter, eliminating any

roughness associated with the real trend in the scenario. In limit states, a value of 1 means that

201 fluctuations are similar to the unfiltered dataset, and therefore no improvement has been

202 achieved; a value of 0 suggests the slope of a scenario remains unchanged and indicates a linear

203 trend. Because all of the scenarios, except the first, include trends showing concavity or convexity,

204 a residual value for the roughness factor would be expected in the lowest limit state, meaning that

205 a value of 0 is not necessarily a goal. J_2 was used to infer the minimum value of bandwidth ratio

206 after which no significant change in the fluctuation of results is achieved. Considering the second

207 power in the formulation of J_2, all observations are valid if the scenarios are mirrored (when they

208 vary from 1 to 0, instead of 0 to 1).

209 The filters are not expected to remove all scatter, and the error attributed to the residual scatter

210 can be calculated using the root mean square error (RMSE). Given that velocity values are usually

211 used as thresholds in an EWS, one concern is whether the filter should be applied to displacement

212 values or to velocity values derived from unfiltered displacements. To address this issue, two

213 different approaches to filtering were investigated: direct and indirect. As a result, two different

214 approaches using the RMSE were also utilized here.

215 *2.3.1. Direct scatter filtration*

216 Direct filtration means the filter is applied to the diagram of interest. If the filtered displacement

217 values are the goal, and the filter is applied to unfiltered displacement values, then the filtering

218 process is called direct filtration. The same concept applies when velocity values are derived

219 using unfiltered displacements and the filters are then directly applied to the velocity values. In

220 this approach, the RMSE follows Eq. 5:

221
$$\text{RMSEd} = \sqrt{\frac{1}{m}\sum_{i=1}^{m}(\widehat{y}_i - y_i)^2},$$
(5)

222 where *RMSEd* is the measurement of error in direct filtration, y_i is the value of the true trend (for

223 the synthetic scenario), $\widehat{y}_i$ is the filtered value, and *m* is the total number of points. This approach

224   is often used in the literature (e.g., Macciotta et al., 2016; Carlà et al., 2017a,b, 2018, 2019; Intrieri

225   et al., 2018).

226   *2.3.2. Indirect scatter filtration*

227   Some EWSs can apply the filter to the displacements but use velocity trends as the metric for

228   evaluation. In this case, the filtered velocity values will be computed using the filtered

229   displacements. Indirect filtration indicates the diagram of interest is the first derivative of the

230   diagram to which the filter is applied. The RMSE in this case is defined as:

231
$$\text{RMSEi} = \sqrt{\frac{1}{m} \sum_{i=1}^{m} (\hat{y}_i' - y_i')^2},$$
(6)

232   where *RMSEi* is the measurement of error in indirect filtration, y_i' is the first derivative of the true

233   trend, $\hat{y}_i'$ is the first derivative of filtered data (derived velocity after the filter is applied to the

234   displacements), and *m* is the total number of points. Similar to J_2, all observations are valid for

235   the mirrored scenarios of those presented in Fig. 1. This is a consequence of using the second

236   power in the definition of *RMSEi* and *RMSEd*.

237   **2.4 Lag Quantification**

238   Only antecedent measurements are fed into the filters, which is expected to result in a lag between

239   the true trend and its identification by the filters. This lag means the calculated value of velocity

240   or displacement occurred sometime in the past. Consequently, reducing this lag means less time

241   is lost with respect to providing an early warning. To quantify the induced lag, the filtered diagrams

242   of all scenarios at all *n/t* ratios and bandwidth ratio values were shifted backwards a number of

243   points equivalent to 0.001 (0.1%) to 0.1 (10%) of all generated points. We refer to this as the shift

244   ratio in the rest of this paper. This shift of filtered diagrams is expected to increase their similarity

245   with the true trend until the best correlation is achieved. The R^2 test was used to determine how

246   well the shifted and filtered results replicate the underlying trend.

2.5. Geocubes Differential GNSS System

247

248 A Geocubes system is a network of differential global navigation satellite system (GNSS) units

249 that works with a single frequency (1572.42 MHz), making it cost-effective (Dorberstein, 2011;

250 Benoit et al., 2014; Rodriguez et al., 2018). Geocubes communicate with each other through radio

251 frequency, and a reference unit outside the boundaries of the landslide is assumed as static for

252 differential correction to increase the poor accuracy associated with single frequency GNSSs

253 (Benoit et al., 2014; Rodriguez et al., 2018). The ability of this system to achieve real-time

254 positioning, remote data collection, and processing makes it a suitable candidate for incorporation

255 into an EWS. As a result, Geocube data are used in this study to evaluate the performance of the

256 three mentioned filters.

2.6. Outlier Detection

257

258 Outliers are defined herein as abnormal inconsistencies (e.g., displacement directions,

259 magnitudes) when compared to the majority of observations in a random sampling of data (Zimek

260 and Filzmoser, 2018). Techniques for outlier detection have been proposed based on the

261 statistical characteristics of datasets. One common example is the Z-score method, which

262 calculates the mean and standard deviation of data within a defined interval and identifies outlier

263 data as those beyond three standard deviations from the mean (Rousseeuw and Hubert, 2011).

264 A limitation of this kind of approach is the sensitivity of the mean and standard deviation to the

265 outlier data points, which has led to the development of other methods that use other indices such

266 as the median (Salgado et al., 2016). One such technique that was adopted in this study is the

267 Hampel filter (Hampel, 1971). In this method, the median of the displacement measurements

268 within a running bandwidth is calculated and data outside a defined threshold from the median

269 are identified as outliers. The threshold is defined as a constant (threshold factor) multiplied by

270 the median absolute deviation. An asymmetric window with a bandwidth ratio of 0.004 (0.4%) and

271 a threshold factor of three were adopted following previous studies (Davies and Gather, 1993;

272   Pearson, 2002; Liu et al., 2004; Yao et al., 2019). The data identified as outliers were then

273   removed from the dataset.

274   **3. Study Site – Ten-mile Landslide**

275   The Ten-mile landslide is located in southwestern British Columbia (BC), in the Fraser River

276   Valley north of Lillooet (Fig. 5a). It is a reactivated portion of a post-glacial earthflow (Bovis, 1985)

277   that was first recognized in the 1970s. The landslide velocity has increased from an average of 1

278   mm/day in 2006 to 6 mm/day in 2016, with a maximum measured velocity of 10 mm/day (Gaib et

279   al., 2012; BGC Engineering Inc., 2016). The movement of this landslide impacts the integrity of

280   BC Highway 99 and a section of railway operated by Canadian National Railway (CN) (Carlà et

281   al., 2018), with most movement limited to the volume downslope from the railway due to the

282   installation of a retaining wall (Macciotta et al., 2017a). Despite the stabilization work done to date,

283   the uppermost tension crack has retrogressed approximately 200 m in 45 years and is now

284   situated 60 m upslope of the railway track (Macciotta et al., 2017b). The landslide lateral extents

285   have not expanded since 1981 according to the aerial photographs Macciotta et al., 2017b). The

286   Ten-mile landslide is currently approximately 200 m wide, 140 m high, and has a volume of 0.75

287   to 1 million m^3, moving towards the Fraser River on a continuous rupture surface with a dip of

288   about 22 to 24°, which is sub-parallel to the ground surface (Rodriguez et al., 2017; Donati et al.,

289   2020). The elevation of the shear surface and mechanism of the landslide have been inferred

290   from the readings of multiple slope inclinometers installed in 2015 (BGC Engineering Inc., 2015).

291   The bedrock in this region consists of volcanic rocks, such as andesite, dacite, and basalt, and is

292   overlain by Quaternary deposits (Donati et al., 2020; Carlà et al., 2018; Macciotta et al., 2017a).

293   The thickness of the landslide varies between 20 and 40 m and the ground profile from the surface

294   to depth comprises medium to high plastic clays and silts overlying colluvium material and glacial

295   deposits, overlying bedrock (BGC Engineering Inc., 2015). The stratigraphy of the sedimented

296   soils in the landslide area notably varies from one borehole to another and reflects the complex

297   stratigraphy of the earthflow.

298   A total of 11 Geocubes were installed at the Ten-mile landslide in 2016. Fig. 5b is a front view of

299   the landslide showing the locations of the Geocube units. Units 44 and 50 are installed near the

300   uppermost tension crack identified as the current landslide backscarp, unit 69 is 30 m above the

301   backscarp, and unit 39 is used as the reference point. Please note that unit 69 is used as the fixed

302   Geocube, and is not shown in Fig. 5b. The other units are located within the boundaries of the

303   landslide, with a maximum distance between units of 310 m (Rodriguez et al., 2018). The time

304   step between every two consecutive measurements is 60 s. Fig. 6 shows the displacements of

305   units 46 and 47, which were the largest in comparison to other Geocubes.
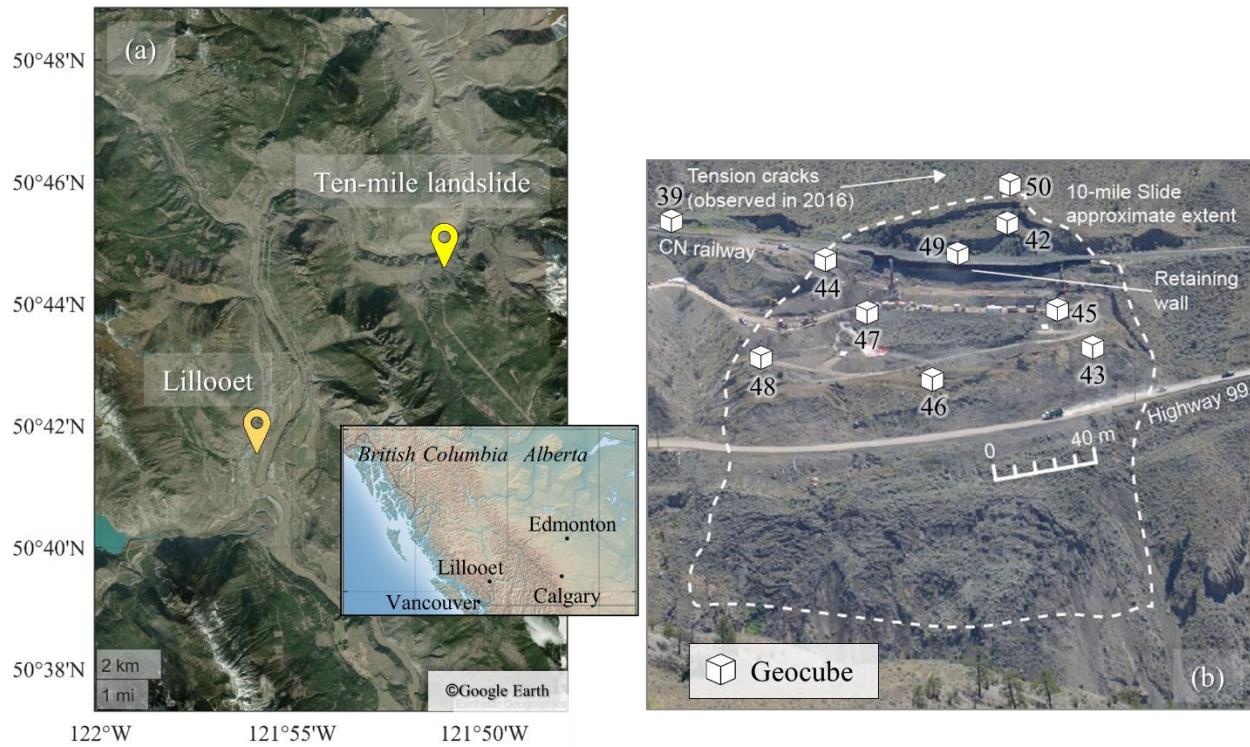
306
307   **Fig. 5** (a) Location of the Ten-mile landslide (© Google Earth) and (b) front view of the Ten-mile landslide
308   and distribution of Geocubes on its surface (Rodriguez et al., 2018; Macciotta et al., 2017b)
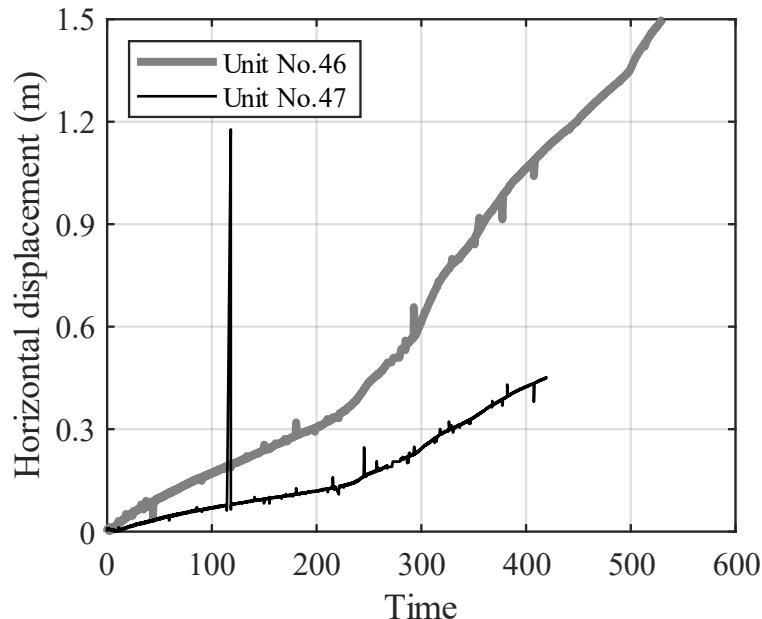
 Fig. 6 *Cumulative horizontal displacement of Geocube units No. 46 and 47*

4. Results

4.1. Synthetic Analysis

Fig. 7 shows the roughness value (J_2) of scenario 6 for SMA, GWMA, and S-G on a semi-

logarithmic scale. This figure illustrates how, regardless of the n/t ratio, J_2 substantially decreases

as the bandwidth ratio increases to 0.01 and then asymptotically approaches a final value. This

means that increasing the bandwidth ratio drastically reduces scatter; however, its effectiveness

is restricted as the bandwidth ratio increases above 0.01. This observation was consistent for

other scenarios. J_2 values (including scenario 6 in Fig. 7) indicate that J_2 approaches its minimum

at bandwidth ratio values of 0.03 to 0.04, regardless of the filter selected.
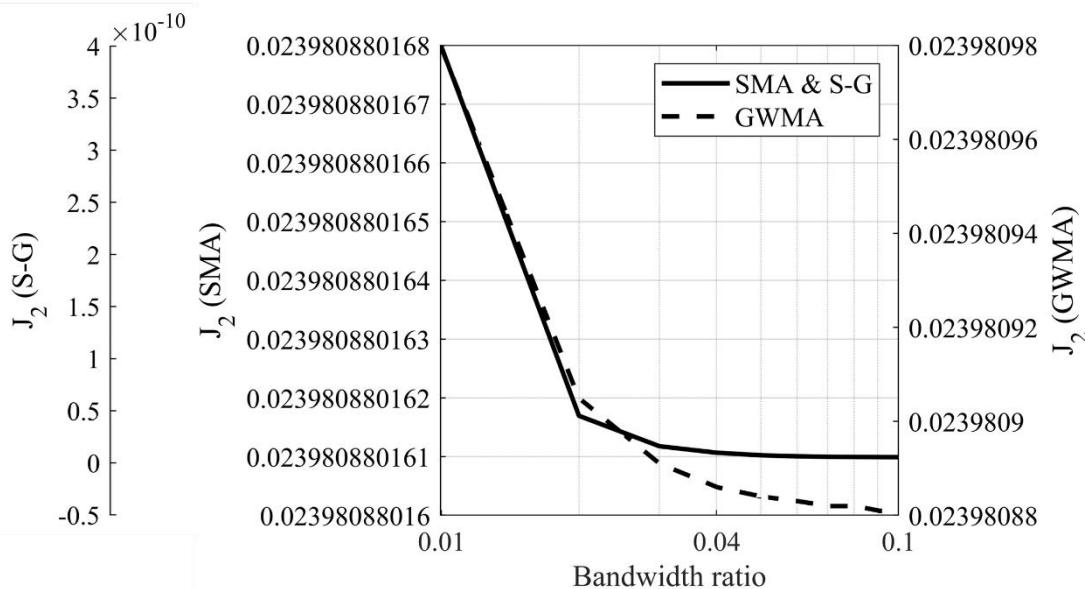
320

321 **Fig. 7** *Variation of roughness factor for scenario 6 with respect to the applied filter on a semi-log scale*

322 *4.1.1. Effect of filters on trend distortion*

323 Scenarios 11 and 12 were first analyzed to evaluate the degree to which the trend was preserved

324 by these filters, as peaks made it easier for visualization. Fig. 8**Error! Reference source not**

325 **found.**a shows the true trend of scenario 11 along with two SMA-filtered scenarios at bandwidth

326 ratios of 0.04 and 0.10, respectively. This figure shows that, as the SMA filter bandwidth

327 increases, the peak in measurements is identified at a later time than the true trend (x=0.5) and

328 the magnitude of the peak is reduced (more than 70% reduction at a bandwidth ratio of 0.10).

329 Furthermore, as the bandwidth ratio increases, the "instantaneous" nature of the peak is lost to a

330 more transitional variation. This highlights a disadvantage of SMA when handling sudden changes

331 in data trends. The calculated *x* value of the peak in scenario 11 is plotted for different bandwidth

332 ratios and for all three filters in Fig. 8**Error! Reference source not found.**b. This figure shows

333 the time at which the peak is identified lags as the bandwidth ratio increases for all filters; however,

334 GWMA and S-G identify the peak with a much smaller lag, independent of the *n*/*t* ratio. As an

335 example, for a year of monitoring data at a frequency of 30 s and bandwidth ratio of 0.10, SMA,

336 GWMA, and S-G predict the peak point approximately 17, 3.5, and 2.7 days after the real peak,

337 respectively. This lag can be attributed to the utilization of an asymmetric window, which leads to

338 a lagged response of the filter. As more points are included in the filtering procedure (increasing

339 bandwidth ratio), this lag increases because the averaging process is sensitive to window type.

340 The degree of sensitivity, however, depends on the filter. Fig. 8**Error! Reference source not**

341 **found.**c shows the variation of the peak magnitude with respect to the bandwidth ratio for all three

342 filters. SMA and GWMA both underestimate the peak value, and the difference between the

343 calculated peak and real peak increases as the bandwidth ratio increases. SMA calculations

344 underestimate the peak more than twice as much as GWMA. On the contrary, S-G intensifies the

345 peak up to a bandwidth ratio of 0.04, with the impact tending to diminish at larger bandwidth ratios;

346 it predicts the true value at a bandwidth ratio value of almost 0.09.
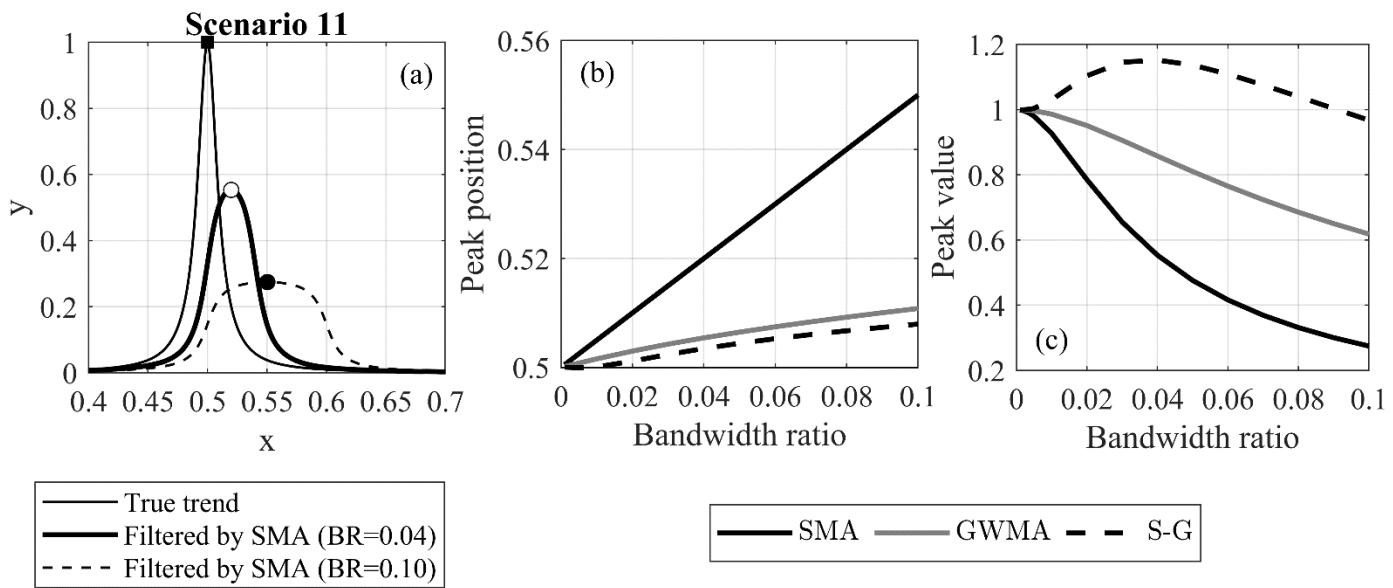
347
348 *Fig. 8 (a) An example of peak displacement by applying SMA, and variation of (b) peak position and (c)*
349 *peak value with respect to the filter and bandwidth ratio used (original peak at 0.5)*

350 Scenario 12 was used for a detailed evaluation of the ability of these filters to conserve the

351 underlying original trend.**Error! Reference source not found.** Fig. 9 shows scenario 12 and the

352 filtered results for all three filters and for an *n*/*t* ratio of 0.15. This scenario and these specific

353 parameters were selected for illustration purposes as they allow visual identification of differences

354 for discussion. The SMA filter considerably underestimates the magnitude of the peak at a

355 bandwidth ratio of 0.04, which should be the minimum bandwidth ratio according to Fig. 7. At a

356 bandwidth ratio of 0.10, the filtered diagram is distorted in comparison to the true trend and the

357   initial peak is not identified. GWMA at a bandwidth ratio of 0.04 shows less underestimation of

358   the peak magnitude, and a slight lag is visually observed at a bandwidth ratio of 0.10. This

359   indicates the significantly better performance of GWMA over SMA. S-G results for both bandwidth

360   ratios closely identify the time and magnitude of both peaks, indicating yet better performance.

361   However, the peak is artificially intensified at a bandwidth ratio of 0.04, and a significant drop

362   occurs well beyond the true trend immediately after the second peak for both bandwidth ratios

363   (pulsating effect), which was also observed in scenario 11. Increasing the degree of the

364   polynomial fitted as part of the S-G methodology was not completely effective at eliminating this

365   effect. The pulsating effect was also observed when a symmetrical window was utilized and is

366   attributed to the negative weights in the S-G kernel.

367
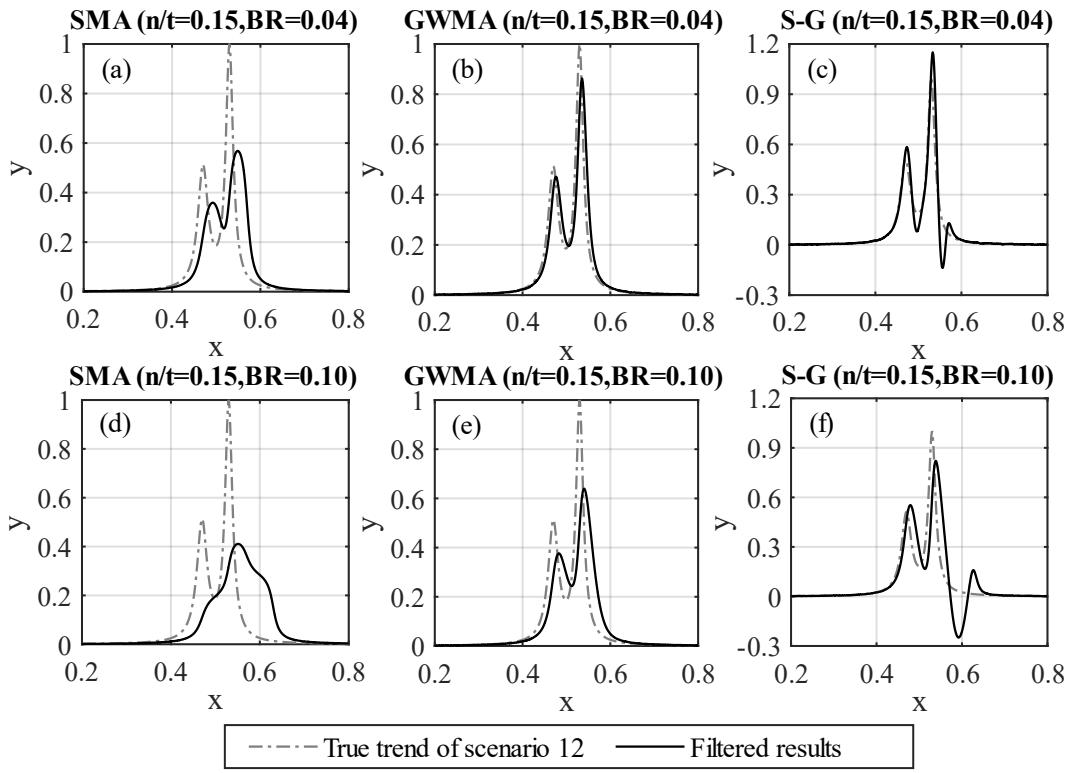
368
369   **Fig. 9** *Filtered results of Scenario 12 with scatter using SMA (a,d), GWMA (b,e), and S-G (c,f) at*
370   *bandwidth ratios (BRs) of 0.04 (a-c) and 0.10 (d-f)*

371   *4.1.2. Results of direct scatter filtration*

372   Fig. 10 shows the RMSEd of all three filters for all of the harmonic synthetic scenarios. This figure

373   shows that, for these numerical analysis on synthetic scenarios, the error depends linearly on the

374   bandwidth ratio for all of the filters and does not depend on the scenario or n/t ratio. SMA shows

375   the greatest difference from the true trend, followed by GWMA (approximately 60% less difference

376   than SMA). S-G, on the other hand, almost lies on the horizontal axis for all of the bandwidth

377   ratios, which means the filtered results yield near zero error. Fig. 10 also shows how the error

378   increases as the bandwidth ratio increases. This can be attributed to the utilization of an

379   asymmetric window, which leads to a lagged response of the filter. As more points are included

380   in the filtering procedure (increasing bandwidth ratio), this lag increases and, consequently,

381   causes larger error. The RMSEd of filters for the instantaneous synthetic scenarios are shown in

382   Fig. 11. In scenario 10, the same behaviour as noted for the harmonic scenarios can be seen fir

383   SMA and GWMA, whereas S-G is not as accurate. This is more noticeable in scenarios 11 and

384   12 in which S-G becomes less accurate than GWMA at larger bandwidth ratios. This result shows

385   that S-G cannot handle the instantaneous scenarios as satisfactorily as the harmonic ones. The

386   errors related to SMA and GWMA for the instantaneous synthetic scenarios show non-linear

387   behavior, and are greater when compared to the harmonic scenarios. Fig. 11 clearly shows all

388   filters are challenged by the instantaneous variations when compared to gradual ones in direct

389   filtration.

390

391
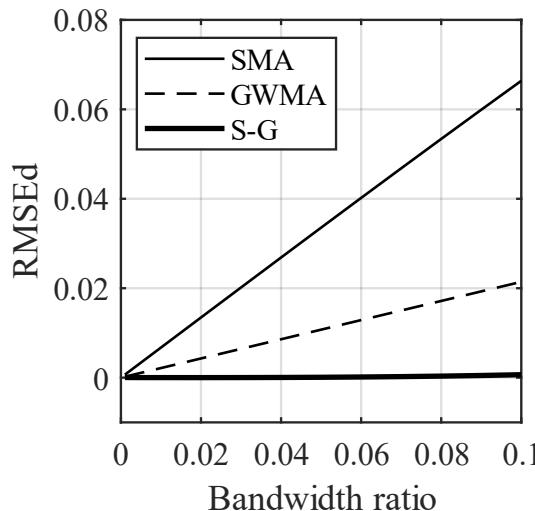
Fig. 10 *RMSEd for the harmonic scenarios*
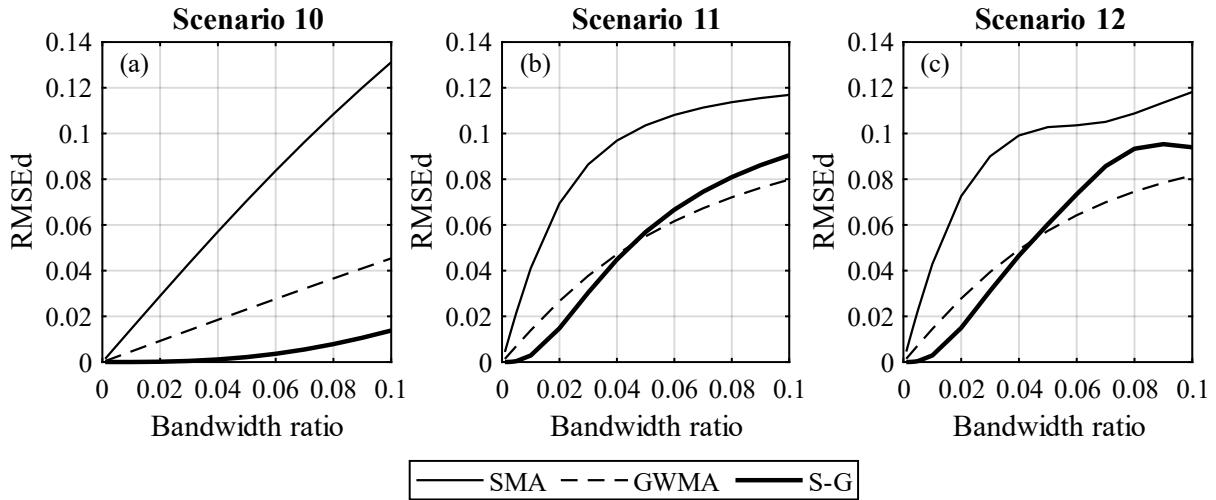
392
393
Fig. 11 *RMSEd for the instantaneous scenarios*

4.1.3. Results of indirect scatter filtration

394

395 Fig. 12 shows the RMSEi results for the harmonic scenarios (when performing indirect filtration)

396 on a semi-logarithmic scale. We observed that the error considerably decreases as the bandwidth

397 ratio increases to 0.02; however, to highlight the variation of error in the range of interest for the

398 bandwidth ratio, only RMSEi values corresponding to bandwidth ratios greater than 0.04 are

399 plotted in Fig. 12 and 13. In Fig. 12, the error for the GWMA is either equal to or slightly less than

400 the error for the SMA, and S-G shows the least error for the harmonic scenarios. The RMSEi

401 results for the instantaneous scenarios (Fig. 13) are similar to those for the harmonic scenarios

402 for large *n/t* ratios (0.05, 0.10 and 0.15). For small *n/t* ratios, the GWMA is superior at bandwidth

403 ratios above 0.06, and S-G has the worst performance.
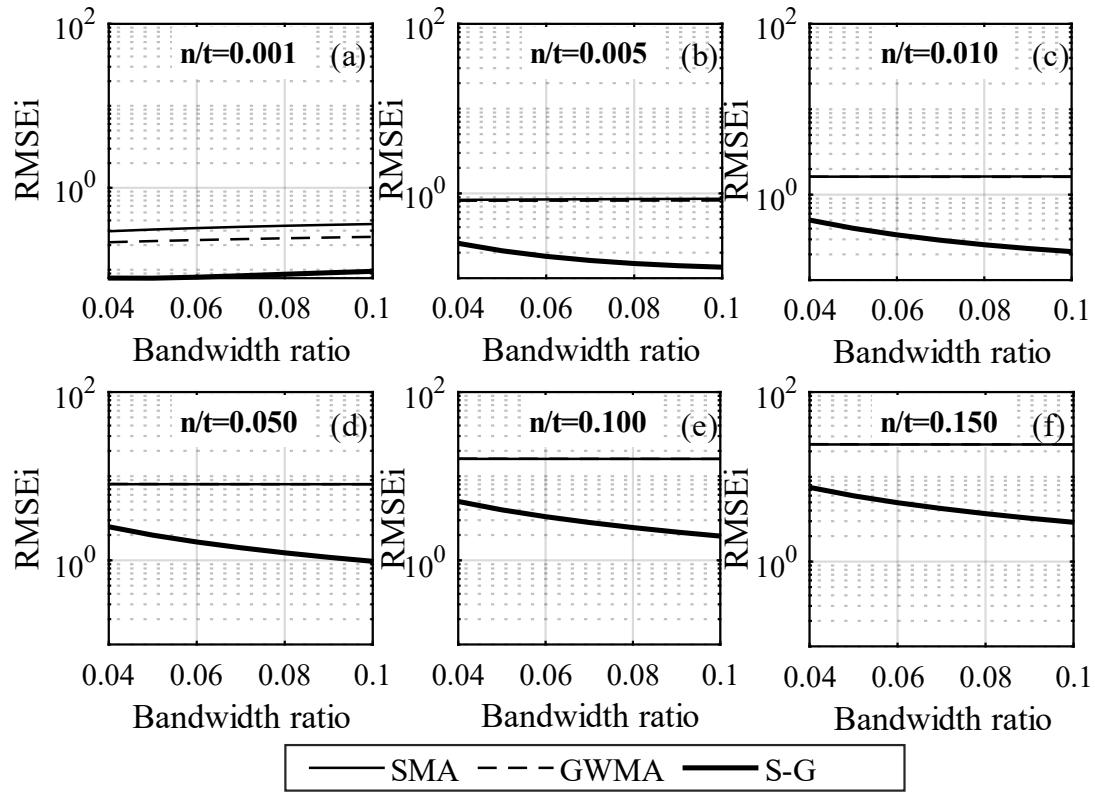
Fig. 12 RMSEi for the harmonic scenarios on a semi-logarithmic scale
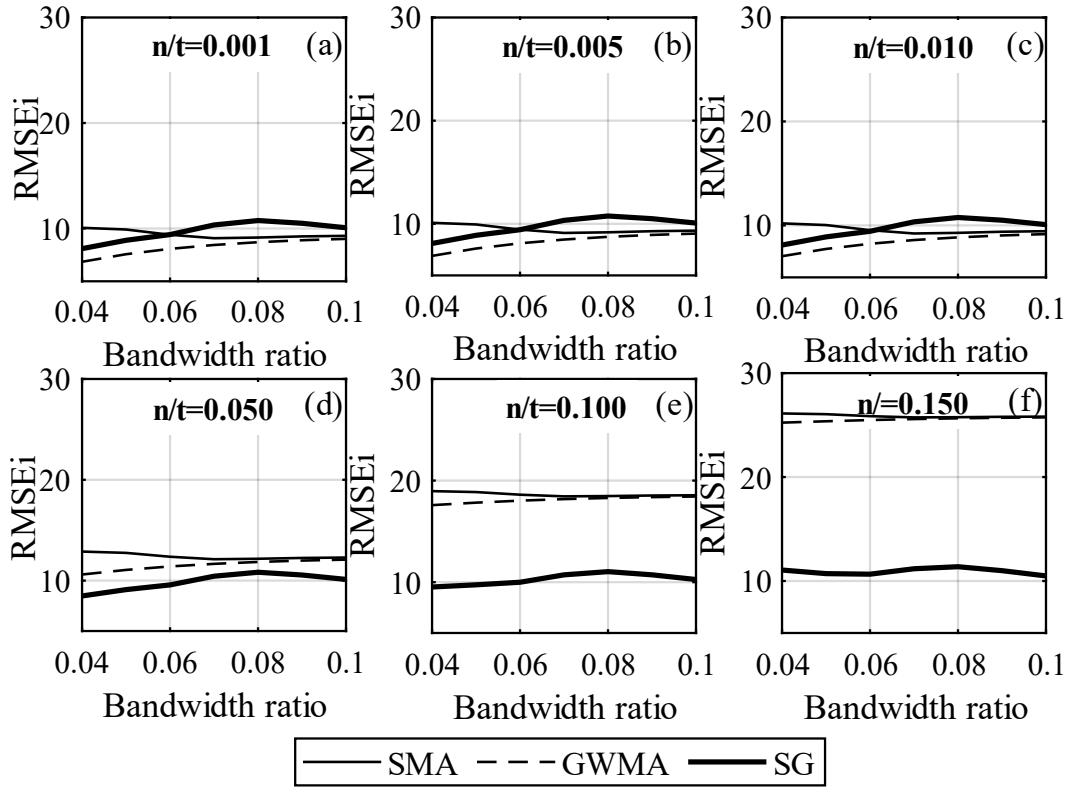
Fig. 13 RMSEi for the instantaneous scenarios

 4.1.4. Lag quantification

409 The non-symmetric inclusion of points causes the identification of a lag in the trend of filtered

410 data. Fig. 14 shows Scenario 10 with respect to the original trend, with scatter added (at an n/t

411 value of 0.15), and the results after filtering with each of the three methods at a bandwidth ratio

412 of 0.04. This figure clearly shows the lag between the results filtered by SMA and GWMA and the

413 true trend. S-G results do not have as severe a lag as that resulting from the other filters; we

414 attribute this to the negative weights in its kernel that anchor the filtered values and prevent a

415 lagged response. A minor pulsating effect can be observed in the S-G filtered data, decreasing

416 the calculated values at a much earlier time than the true trend. This suggests that S-G is robust

417 with respect to identifying initial changes in monitoring trends but overcorrects subsequent

418 changes; SMA grossly lags with respect to the identification of any change; and GWMA has a

419 reduced lag when compared to SMA.
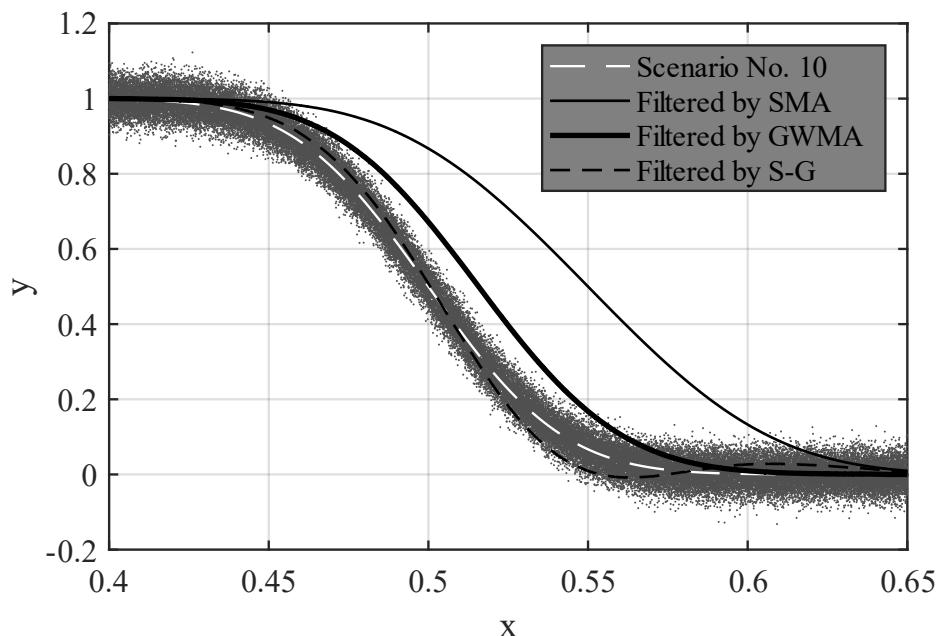
420

421 **Fig. 14** *Scenario 10 with and without scatter, and with scattered results filtered by SMA, GWMA, and S-G*
422 *for an n/t value of 0.15 and a bandwidth ratio of 0.04.*

423 Fig. 15a shows an example of R^2 correlation for scenario 7, comparing the original trend and the

424 results filtered by SMA at an n/t value of 0.01 and bandwidth ratio of 0.04. The shift ratio is the

425   shift of filtered trends (in the horizontal axis – parameter x) relative to the range of x values. R^2

426   calculations are shown for the filtered data (shift ratio of 0) and as the filtered trends are shifted

427   backwards in time (negative shift ratio valus). In this analysis, the peak R^2 value (largest

428   correlation between the shifted filtered results and original trend) indicates the shift required to

429   minimize the lag in identifying the original trend changes, therefore providing a quantitative

430   approach to calculating the lag in parameter x. In the example in Fig. 15a, the lag corresponded

431   to 0.018 (1.8%) of the total points.
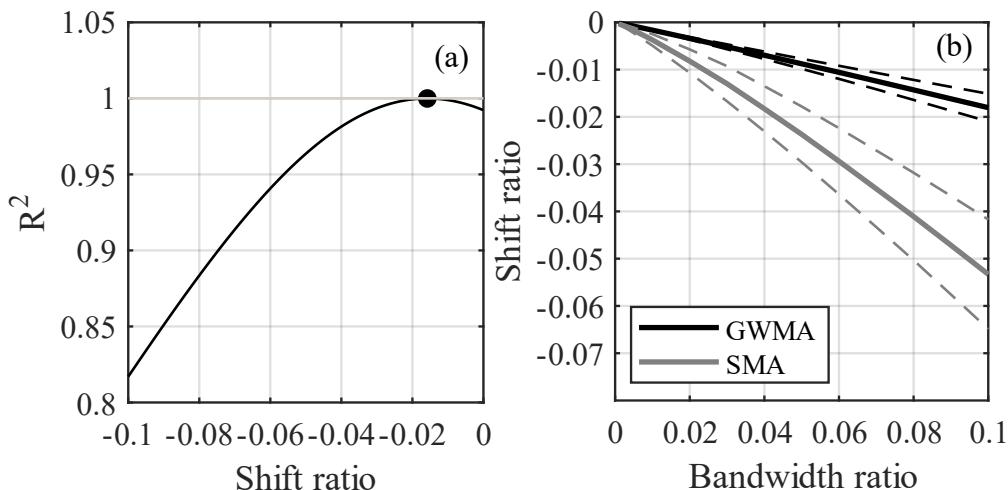
432
433   ***Fig. 15** (a) R^2 values for scenario 7 with filtered and shifted results at an n/t value of 0.01 and bandwidth*
434   *ratio of 0.04 and (b) shift ratio at peak R^2 for all scenarios and n/t ratios, with the mean (solid line)*
435   *bounded by one standard deviation (dashed lines)*

436   Peak R^2 values for all scenarios and n/t values are closely correlated with the bandwidth ratio.

437   The lag, quantified by the shift ratio, is larger when the trend change is more pronounced;

438   therefore, the correlation between the shift ratio and bandwidth ratio is different for different

439   scenarios. Fig. 15b shows the mean correlation between the shift ratio and bandwidth ratio, for

440   all scenarios and n/t values, bounded by one standard deviation, for GWMA and SMA. Table 2

441   shows linear and quadratic regressions of this correlation and the strength of the correlation in

442   terms of R^2 and RMSE. Fig. 15b quantitatively shows that GWMA lags less than SMA with respect

443   to identifying changes in measurement trends. Moreover, the uncertainty associated with lag for

444   SMA is greater than for GWMA because of the larger standard deviation. Fig. 15b quantifies how

445   increasing the bandwidth ratio increases the lag with respect to identifying true measurement

446   trends and, although large bandwidth ratios decrease the scatter in data, the bandwidth ratio

447   should carefully balance minimizing both scatter (J_2) and lag (shift ratio). S-G is not included in

448   this analysis as the method resulted in no significant lag in identifying changes in measurement

449   trends; however, it had the disadvantages previously noted including pulsating effects and

450   overestimating peak values.

451   **Table 2** *Regression correlations between shift ratio (SR) and bandwidth ratio (BR) with the strength of the*
452   *correlation in terms of R^2 and RMSE*

	Linear regression		Quadratic regression	
SMA	SR=-0.5087(BR)	R^2=0.9940 RMSE=0.0014	SR=-1.323(BR^2)-0.4049(BR)	R^2=0.9997 RMSE=3.24E-4
GWMA	SR=-0.1783(BR)	R^2=0.9996 RMSE=1.2963E-4	SR=-0.1171(BR^2)-0.1691(BR)	R^2=0.9999 RMSE=3.5672E-5

453   **4.2. Results on the Ten-mile landslide**

454   Unfiltered results reported by Geocubes 46 and 47 installed on the Ten-mile landslide were

455   processed by all three filters. To illustrate to the reader through visual inspection the difference

456   between the performance of SMA, GWMA, and S-G, only a 200-day window of displacement data

457   from Geocube 46 and filtered points produced by direct filtration are shown in Fig. 16. Fig. 16a

458   also features an inset showing scaled scenario 4, which resembles the general trend of Geocube

459   46 data for the period from day 200 to 400. Fig. 16 shows that increasing the bandwidth ratio

460   reduces the scatter, but increases the lag in the filtered results, consistent with observations on

461   the synthetic datasets. For bandwidth ratios larger than 0.04, SMA becomes insensitive to some

462   short-scale (20- to 30-day) trends in the data (qualitative visual inspection). As an example, at a

463   bandwidth ratio of 0.10, SMA suggests the displacement of Geocube 46 follows a bi-linear trend

464   with an inflection point at day 240, while unfiltered points and other filters suggest other periods

465 of acceleration and deceleration. Importantly, S-G is sensitive to even subtle variation and does

466 not show significant lag.
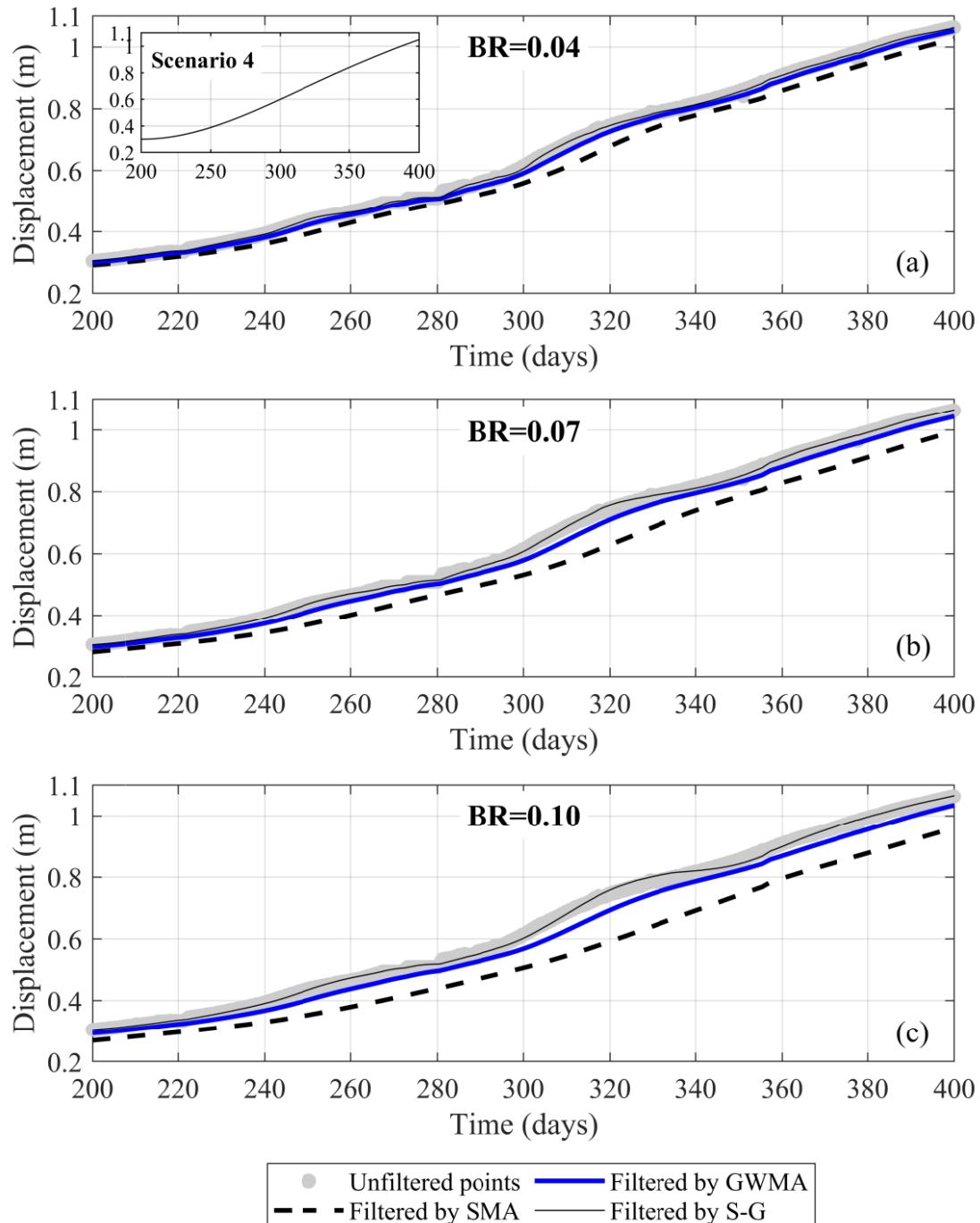
467
468 **Fig. 16** *Unfiltered displacement of Geocube 46 data vs. time and data filtered by SMA, GWMA, and S-G*
469 *for bandwidth ratios (BRs) of (a) 0.04, (b) 0.07, and (c) 0.10.*

470 Fig. 17 shows the filtered velocity values obtained by directly filtering the calculated velocities and

471 by indirectly filtering the displacement values before calculating the velocity from Geocube 46

472   data. The direct and indirect filtering approaches demonstrated similar performance in terms of

473   scatter reduction for Geocube 46 data. As the bandwidth ratio increases, SMA tends to

474   significantly attenuate the local maximum and minimum points in comparison to results at smaller

475   bandwidth ratios, indicating a probable loss of information about the landslide behaviour and

476   sensitivity of this filter to the bandwidth ratio, as also noted in Fig. 16 (curvature loss in SMA

477   results). Indirect filtration by SMA seems to be limited near the boundary at time zero, resulting in

478   a subdued replica of direct filtration. The length of this region is found to be governed by the

479   bandwidth ratio, as the necessary number of points for filtering in this portion has not been

480   provided to the filter. This is also observed in S-G results. This problem was not found in GWMA

481   results, as direct and indirect filtration both follow the same pattern. GWMA and S-G are both able

482   to preserve the velocity variation even at the most intense filtration (bandwidth ratio of 0.10);

483   however, variations between local maxima and minima are more extreme in S-G than GWMA

484   results. This is attributed to peak overestimation (Fig. 8 and 9) or a pulsating effect superimposing

485   on the peaks/troughs. Moreover, the S-G results still demonstrate relatively large fluctuations

486   even at the largest bandwidth ratio. This means that application of S-G might still trigger false

487   alarms in an EWS if the landslide is moving at a faster rate or experiencing different episodes of

488   acceleration and deceleration. To avoid this, a larger bandwidth ratio should be used but this can

489   be problematic due to the higher computational effort required and issues that might follow, such

490   as the pulsating effect.

491   Results for Geocube 47 confirm the same observations made for Geocube 46 but also allow for

492   an evaluation of the significance of outliers on the filtered results. Fig. 18a displays the outliers

493   detected in the displacement diagram of Geocube 47 data along with the threshold established

494   by the Hampel algorithm using an asymmetric window, bandwidth of 0.4% and threshold factor of

495   3. Fig. 18b-d shows a magnified portion of the displacement measurements for Geocube 47

496   filtered by each of the three filters at three different bandwidth ratios before the elimination of

497   outliers. This highlights the necessity of outlier elimination before application of any scatter filter.

498   These plots show that detecting and removing outliers significantly impacts the performance of

499   S-G, as the presence of the outlier generates a peak that follows the outlier measurement and is

500   followed by a sudden decrease that drops well beyond the data trend. SMA tends to widen the

501   time range affected by the outlier more than GWMA but, for most part, the SMA-filtered results

502   are almost parallel to the underlying trend. All filters appear to be significantly impacted by the

503   outlier value, suggesting a pre-processing filter is required to remove outliers regardless of the

504   use of SMA, GWMA, or S-G to reduce scatter. The outliers were successfully identified and

505   removed after application of the Hampel algorithm, and the above-mentioned effects were no

506   longer observed in the filtered results.
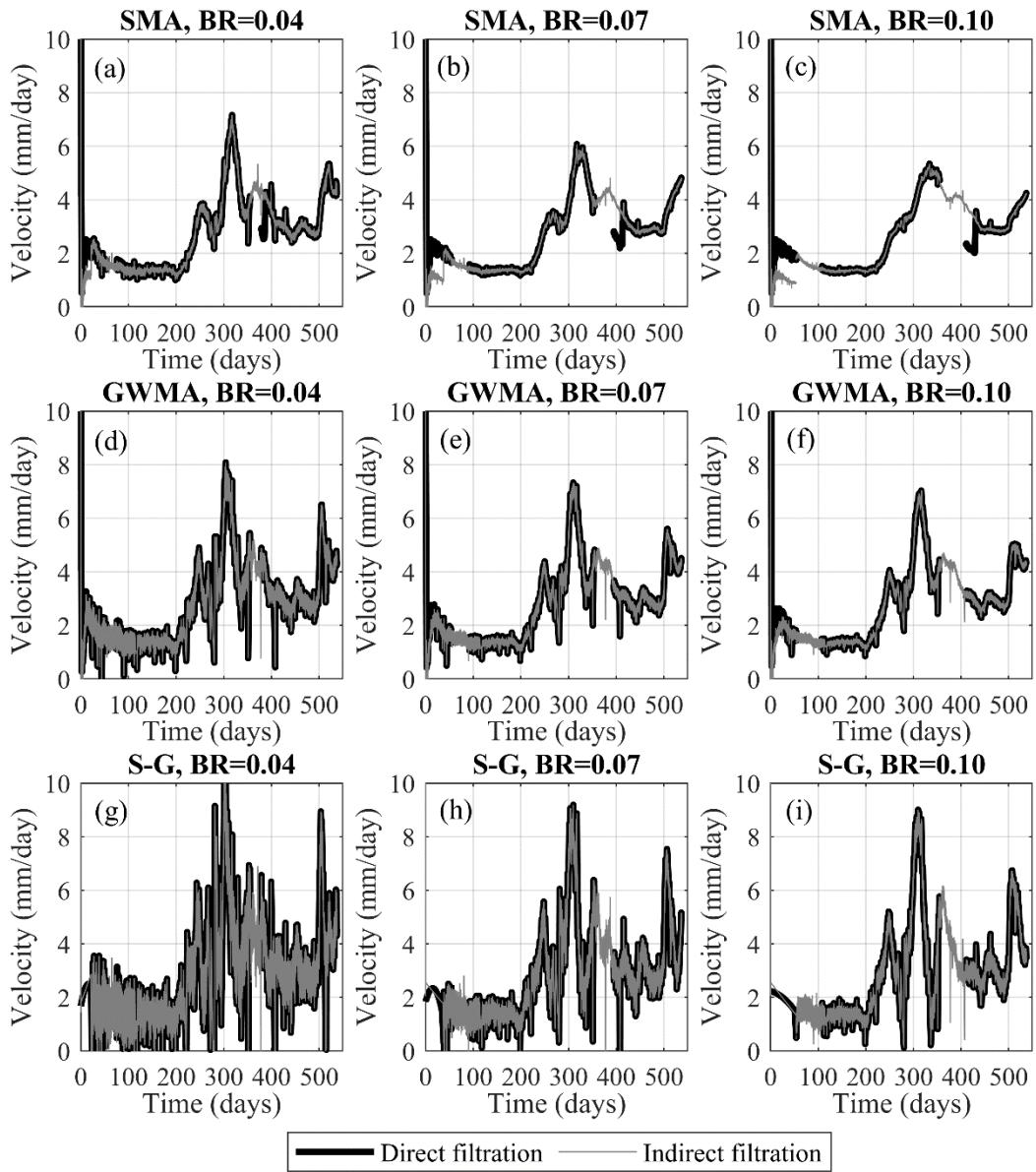
507
Fig. 17 *Indirect and direct filtration results of Geocube No. 46 velocity values for bandwidth ratio (BR)*
509 *values of (a) 0.04, (b) 0.07, and (c) 0.10.*
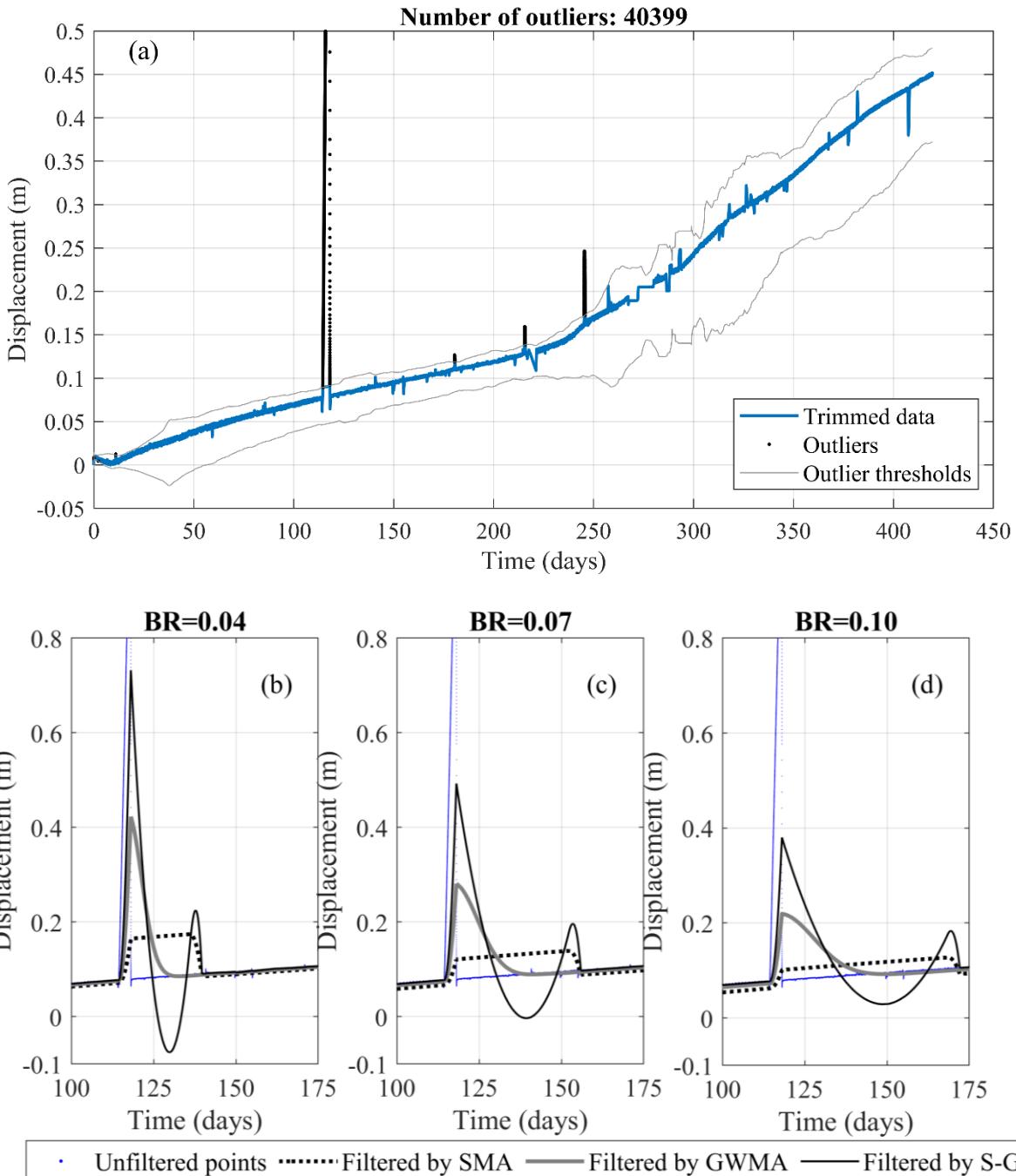
Fig. 18 Unfiltered and filtered displacement measurements for Geocube 47 at bandwidth ratios (BRs) of (a) 0.04, (b) 0.07 and (c) 0.10

4.2.1. Lag minimization in filtered Geocube results

The lag between unfiltered and filtered data for Geocube 46 (Fig. 16) is consistent with the synthetic database results. The lag quantification results (Fig. 15b) were used to provide a correction value for the filtered Geocube results. The shift ratios used for this purpose with respect

518 to each filter and bandwidth ratio are tabulated in Table 3. To determine whether the results of

519 lag correction using the mean correlations derived from the synthetic scenarios (Table 2) were

520 acceptable, the filtered diagrams were shifted (using the mean line for GWMA and values

521 between the mean and lower boundary for SMA) and different portions of the displacement

522 diagrams for Geocubes 46 and 47 were examined. Some examples are shown in Fig. 19

Bandwidth ratio	Shift ratio	
	SMA	GWMA
0.04	-0.02	-0.007
0.07	-0.035	-0.012
0.10	-0.06	-0.018

523 . The mean and standard deviation of the scatter around the trend (error distribution) were

524 calculated by assuming a linear trend within the short time periods of analysis (considered an

525 approximation of the true displacement trend for the short time interval). These were also

526 calculated for the filtered and shifted diagrams. The closer the mean and standard deviation of

527 the filtered and shifted data are to that obtained from the linear trend, the better the performance

528 of the lag correction based on the results from the synthetic scenarios. As an example, for the

529 time period from day 250 to 260, the GWMA resulted in a standard deviation of 0.001 to 0.0015

530 for bandwidth ratios from 0.04 to 0.10, respectively; corresponding values for SMA to 0.0018 to

531 0.0021. This illustrates that shifted GWMA results are closer to the true (scatter-free)

532 displacements because the standard deviations of scatter inferred by this filter are closer to the

533 true scatter, although both have good agreement with the true scatter. The means of inferred

534 scatter by both filters are also close enough to the mean of the true scatter (almost zero). The

535 results show the statistical indices of scatter inferred from the filtered shifted displacement

536 measurements closely agree with that considered to be true scatter, and therefore the filtered

537 displacement measurements are corrected for lag. This suggests the correlations stated in Fig.

538   15b and Table 2 based on the synthetic scenarios are applicable to minimize the lag for the

539   Geocube system at the Ten-mile landslide.

540   ***Table 3.*** *Shift ratios used for lag minimization of Geocube 46 displacements*

Bandwidth ratio	Shift ratio	
	SMA	GWMA
0.04	-0.02	-0.007
0.07	-0.035	-0.012
0.10	-0.06	-0.018

541
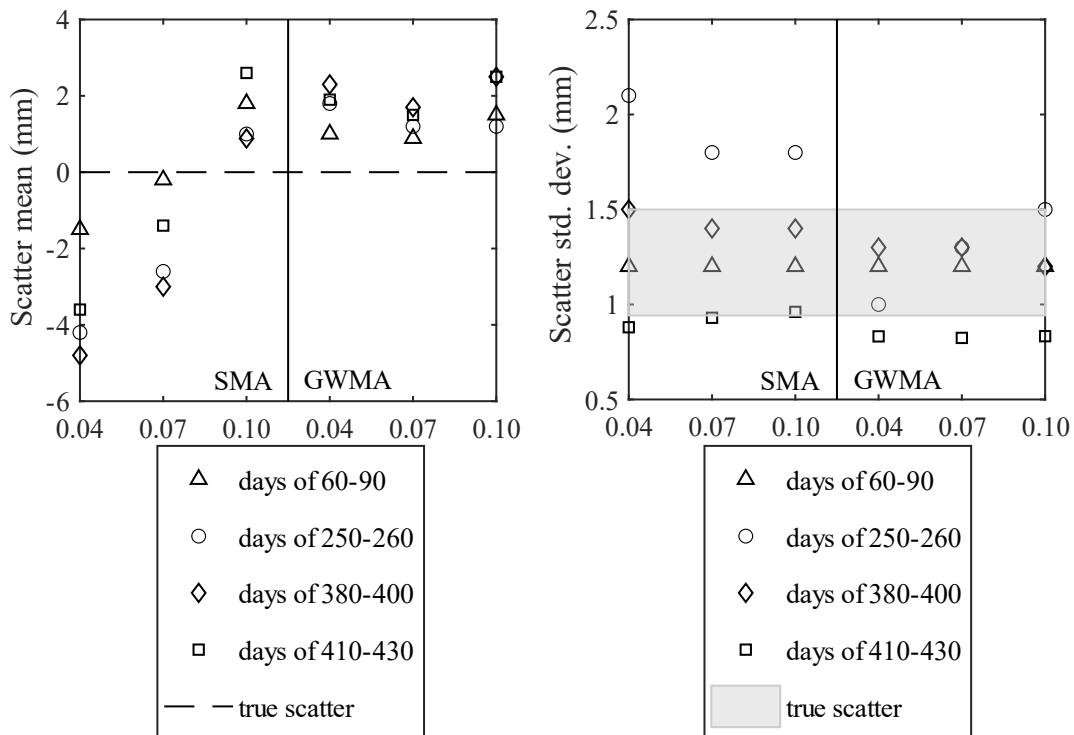
542
543   ***Fig. 19.*** *Mean and standard deviation of scatter inferred by SMA and GWMA in comparison with true*
544   *scatter in the displacement of Geocube 46*

545

5. Discussion

547   Previous studies dedicated to landslide monitoring consistently adopt SMA for scatter

548   minimization in displacement data. However, the adequacy of this filter and the effect of

549 bandwidth selection were not well understood. Analyzes conducted on synthetic databases in this

550 study using a roughness factor (J_2) demonstrate that at least 4% of the total observations should

551 be fed into the filter to ensure fluctuations are sufficiently reduced.

552 The results of this study show that SMA tends to considerably distort the underlying trend at a

553 bandwidth ratio of 0.10 (Fig. 8 and 9), and its lagged response with respect to real-time monitoring

554 is almost three times that of GWMA results. As a result, a bandwidth ratio between 0.04 and 0.07

555 is suggested. However, we caution that the bandwidth should be selected with a complete

556 awareness that SMA is highly sensitive to bandwidth, and sensitivity analyses on bandwidth are

557 recommended when defining an EWS. Corresponding observations were made during the

558 analysis of displacement data from Geocubes installed on the Ten-mile landslide.

559 Error calculations show that GWMA and S-G outperform SMA in both direct and indirect filtration

560 and are more successful in preserving the true displacement trend. The near-zero lagged

561 response of S-G makes it a notable candidate for developing an EWS. Nonetheless, its intrinsic

562 shortcoming in handling peaks, leading to a pulsating effect, will pose challenges for its utilization.

563 The bandwidth range used for SMA is also suggested to be applied with the S-G filter.

564 GWMA results suggest a proper trade-off can be achieved between minimizing the lag time and

565 scatter and avoiding the pulsating effect. Compared to SMA and S-G, GWMA is less sensitive to

566 changes in the bandwidth. Analyses focused on the Geocube data also confirm that GWMA is

567 capable of constraining the fluctuations in the velocity diagram while not attenuating variations in

568 the displacement rate diagram. Moreover, the lag quantification chart proposed could reliably

569 capture the required shift with a greater degree of confidence in comparison to SMA even at the

570 largest bandwidth ratio studied here (0.10). The bandwidth for GWMA can therefore range of 0.04

571 to 0.10. Moreover, we observed consistency between direct and indirect filtration results using

572 GWMA but greater differences when using SMA or S-G results. This was especially the case in

573   the early parts of the datasets and at some locations where outlier elimination was likely

574   ineffective.

575   Filter and bandwidth selections should not be arbitrarily or purely empirical, as differences in

576   outcomes can be substantial. An automated surveillance system for landslides demands stability

577   in filter performance for a variety of circumstances, considering the ground can experience

578   irregular sequences of acceleration and deceleration. The results here suggest practice moves

579   away from the adoption of SMA due to the limitations discussed. S-G demonstrates some

580   inconsistent or erratic performance for certain displacement trends, which is detrimental although

581   overall the error is smaller than for SMA. On the balance of its strengths and limitations as

582   evaluated in this study, GWMA appears to be the more robust approach.

583   **6. Conclusions**

584   This study evaluated the suitability of SMA, GWMA, and S-G filters for scatter reduction of

585   datasets targeted for use in an EWS. A total of different 12 scenarios with harmonic and

586   instantaneous changes were synthetically generated and random variations with Gaussian

587   distribution then added to produce unfiltered results. The three filters considered were then each

588   applied with different bandwidths and the error computed. These filters were also successfully

589   applied to the records from two Geocubes installed on the Ten-mile landslide. The results led to

590   the following conclusions:

591   •   When used for direct filtration of harmonic scenarios, the error resulting from the GWMA

592   approach is approximately one-third that of the SMA approach. The S-G approach results

593   in near zero error regardless of the values of the bandwidth ratio and n/t. When used for

594   direct filtration of instantaneous scenarios, the superiority of S-G is no longer unconditional

595   and depends on the bandwidth ratio; this reflects the fact that S-G cannot appropriately

596   handle peaks in the velocity diagram.

597 • When used for indirect filtration of harmonic scenarios, S-G again outperforms the other
598 methods. The error associated with GWMA is marginally less than for SMA. These
599 observations are not valid when the filters are applied to instantaneous scenarios, as
600 GWMA results in less error than S-G at bandwidth ratios above 0.03.

601 • Detailed investigations with scenarios 11 and 12 demonstrate that that SMA distorts the
602 underlying trend by displacing and sometimes neglecting peak(s), while GWMA and S-G
603 tend to preserve them somewhat similarly.

604 • Due to the presence of negative weights in the S-G kernel, some artificial smaller troughs
605 and peaks are created after major peaks. This phenomenon, referred to herein as a
606 pulsating effect, results in unfavorable performance of S-G on the velocity and
607 displacement diagrams, especially in the presence of outliers.

608 • Investigations on the roughness factor reveal the bandwidth ratio should be at least 0.04.
609 Taking this into account, GWMA seems to be the most reasonable option as the related
610 uncertainties are much smaller than for S-G and the error is acceptable and less than for
611 SMA.

612 • A consequence of using asymmetric windows in the filtering process is a lag in the SMA
613 and GWMA results that increases with increasing bandwidth ratio. Lag quantification
614 suggests a correlation between the needed shift and bandwidth ratio that can be used to
615 eliminate the lag. SMA requires approximately three times the shift of GWMA on average.

616 • Application of these filters to displacement data reported by Geocubes shows SMA and
617 S-G are unable to properly handle data points at the beginning of the dataset (i.e., near
618 the boundary) in indirect filtration of the velocity diagram. Moreover, SMA and S-G are
619 inclined to respectively underestimate and overestimate peaks and fluctuations in the
620 velocity diagram. Overall, GWMA provides the most reliable filtered values for velocity with
621 no distinct difference between direct and indirect filtration.

622 **Appendix A**

623   Consider a polynomial of degree k that is intended to be fitted over an odd number of points

624   denoted as z. The weighting coefficients of the Savitzky-Golay filter can be extracted from the first

625   row of matrix C (Eq. 7):

626
$$C=(J^TJ)^{-1}J^T, \tag{7}$$

627   where T operator is the transpose of a matrix and J is the Vandermonde matrix, with elements at

628   the ith row and jth column ($1 \leq i \leq z$ and $1 \leq j \leq k+1$) that can be achieved as follows:

629
$$J_{ij}=m_i^{j-1}, \tag{8}$$

630   where m is the local index of points ($-(z+1)/2 \leq m \leq (z+1)/2$). As an example, the kernel of an S-G

631   filter that fits a quadratic polynomial ($k=2$) over seven points ($z=7$) is attained here. In the first

632   step, J is set up as follows:

633
$$J=\begin{bmatrix} 1 & (-3)^1 & (-3)^2 \\ 1 & (-2)^1 & (-2)^2 \\ 1 & (-1)^1 & (-1)^2 \\ 1 & (0)^1 & (0)^2 \\ 1 & (1)^1 & (1)^2 \\ 1 & (2)^1 & (2)^2 \\ 1 & (3)^1 & (3)^2 \end{bmatrix}. \tag{9}$$

634   Then, using Eq. 1, matrix C is computed as Eq. 10:

635
$$C=\begin{bmatrix} -0.0952 & 0.1429 & 0.2857 & 0.3333 & 0.2857 & 0.1429 & -0.0952 \\ -0.1070 & -0.0714 & -0.0357 & 0 & 0.0357 & 0.0714 & 0.1071 \\ -0.0595 & 0 & -0.0357 & -0.0476 & -0.0357 & 0 & 0.0595 \end{bmatrix}. \tag{10}$$

636   The second and third rows of C are the coefficients to find the filtered values' first and second

637   derivations at the point of interest, respectively.

638   **Data availability**

639   The synthetic database can be generated through the comprehensive steps provided here. The

640   Geocube measurements of the Ten-mile landslide displacement are not publicly available.

Author contribution

Sohrab Sharifi: conceptualization, methodology, analysis, writing – draft preparation. Michael Hendry: supervision, review, writing – review and editing, project administration. Renato Macciotta: supervision, review, writing – review and editing. Trevor Evans: writing – review and editing, validation, project administration.

Competing interests

The authors declare that they have no conflict of interest.

Acknowledgment

The authors thank Canadian National Railway (CN) for providing access to the Ten-mile site and for purchasing the Geocube units. This research was conducted through the (Canadian) Railway Ground Hazard Research Program, which is funded by the Natural Sciences and Engineering Research Council of Canada (NSERC ALLRP 549684-19), Canadian Pacific Railway, CN, and Transport Canada.

References

Atzeni, C., Barla, M., Pieraccini, M., and Antolini, F.: Early warning monitoring of natural and engineered slopes with ground-based synthetic-aperture radar, Rock Mech. Rock Eng., 48(1), 235-246, https://doi.org/10.1007/s00603-014-0554-4, 2015.

Benoit, L., Briole, P., Martin, O., and Thom, C.: Real-time deformation monitoring by a wireless network of a low-cost GPS, J. Appl. Geodesy, 8(2), 119-128, 2014.

Benoit, L., Briole, P., Martin, O., Thom, C., Malet, J. P., and Ulrich, P.: Monitoring landslide displacements with the Geocube wireless network of low-cost GPS, Eng. Geol., 195, 111-121, 2015.

663 BGC Engineering Inc. CN Lillooet Sub. M. 167.7 (Fountain Slide) September 2015 Drilling and
664 Instrumentation. Project report to Canadian National Railway, 2015.

665 BGC Engineering Inc. CN Lillooet Sub. M. 167.7 (Ten Mile Slide) April 2016 Drilling and
666 Instrumentation. Project report to Canadian National Railway, 2016.

667 Bovis, M. J.: Earthflows in the interior plateau, southwest British Columbia, Can. Geotech. J.,
668 22(3), 313-334, 1985.

669 Bozzano, F., Mazzanti, P., and Moretto, S.: Discussion to: 'Guidelines on the use of inverse
670 velocity method as a tool for setting alarm thresholds and forecasting landslides and structure
671 collapses' by T. Carlà, E. Intrieri, F. Di Traglia, T. Nolesini, G. Gigli, and N.
672 Casagli, Landslides, 15(7), 1437-1441, 2018.

673 Carlà, T., Farina, P., Intrieri, E., Botsialas, K., and Casagli, N.: On the monitoring and early-
674 warning of brittle slope failures in hard rock masses: Examples from an open-pit mine, Eng.
675 Geol., 228, 71-81, 2017a.

676 Carlà, T., Intrieri, E., Di Traglia, F., Nolesini, T., Gigli, G., and Casagli, N.: Guidelines on the use
677 of inverse velocity method as a tool for setting alarm thresholds and forecasting landslides and
678 structure collapses, Landslides 14(2), 517-534, 2017b.

679 Carlà, T., Macciotta, R., Hendry, M., Martin, D., Edwards, T., Evans, T., Farina, P., Intrieri, E., and
680 Casagli, N.: Displacement of a landslide retaining wall and application of an enhanced failure
681 forecasting approach, Landslides, 15(3), 489-505, 2018.

682 Carlà, T., Intrieri, E., Raspini, F., Bardi, F., Farina, P., Ferretti, A., Colombo, D., Novali, F., and
683 Casagli, N.: Perspectives on the prediction of catastrophic slope failures from satellite InSAR, Sci.
684 Rep., 9(1), 1-9, 2019.

Carri, A., Valletta, A., Cavalca, E., Savi, R. and Segalini, A.: Advantages of IoT-based geotechnical monitoring systems integrating automatic procedures for data acquisition and elaboration, Sensors, 21(6), 2249, 2021.

Casagli, N., Frodella, W., Morelli, S., Tofani, V., Ciampalini, A., Intrieri, E., Raspini, F., Rossi, G., Tanteri, L., and Lu, P.: Spaceborne, UAV and ground-based remote sensing techniques for landslide mapping, monitoring and early warning, Geoenviron. Disasters, 4(1), 1-23, 2017.

Chae, B. G., Park, H. J., Catani, F., Simoni, A., and Berti, M.: Landslide prediction, monitoring and early warning: a concise review of state-of-the-art, Geosci. J., 21(6), 1033-1070, 2017.

Chen, M., and Jiang, Q.: An early warning system integrating time-of-failure analysis and alert procedure for slope failures, Eng. Geol., 272, 105629, 2020.

Clague, J. J., and Bobrowsky, P. T.: International year of planet earth 8. Natural hazards in Canada, Geosci. Can. 37(1), 17-37, 2010.

Cleveland, W. S.: LOWESS: A program for smoothing scatterplots by robust locally weighted regression, Am. Stat., 35(1), 54, 1981.

Cleveland, W. S., and Devlin, S. J.: Locally weighted regression: an approach analysis by local fitting, J. Am. Stat. Assoc. 83(403), 596-610, 1988.

Clifford, P.: Monte Carlo methods, in: statistical methods for Physical Science, edited by: Stanford, J. L., and Vardeman, S. B., Elsevier, 125-153, 1994.

Davies, L., and Gather, U.: The identification of multiple outliers, J. Am. Stat. Assoc., 88(423), 782-792, 1993.

Deane, E.: The Application of Emerging Monitoring Technologies on Very Slow Vegetated Landslides, Dissertation, University of Alberta, 2020.

707 Desrues, M., Malet, J.P., Brenguier, O., Carrier, A., Mathy, A., and Lorier, L.: Landslide kinematics

708 inferred from in situ measurements: the Cliets rock-slide (Savoie, French Alps), Landslides, 1-16,

709 2021.

710 Dick, G.J., Eberhardt, E., Cabrejo-Liévano, A.G., Stead, D. and Rose, N.D.: Development of an

711 early-warning time-of-failure analysis methodology for open-pit mine slopes utilizing ground-

712 based slope stability radar monitoring data, Canadian Geotechnical Journal, *52*(4), 515-529,

713 2015.

714 Donati, D., Stead, D., Lato, M., and Gaib, S.: Spatio-temporal characterization of slope damage:

715 insights from the Ten Mile Slide, British Columbia, Canada, Landslides, 17(5), 1037-1049, 2020.

716 Dorberstein, D.: Fundamentals of GPS Receivers: A Hardware Approach, Springer Science &

717 Business Media, Nipomo, CA, USA, 2011.

718 Gaib, S., Wilson, B., and Lapointe, E.: Design, construction and monitoring of a test section for

719 the stabilization of an active slide area utilizing soil mixed shear keys installed using cutter soil

720 mixing, Proceedings of the ISSMGE - TC 211 International Symposium on Ground Improvement

721 IS-GI, Brussels, 3, 147-158, 2012.

722 Grebby, S., Sowter, A., Gluyas, J., Toll, D., Gee, D., Athab, A., and Girindran, R.: Advanced

723 analysis of satellite data reveals ground deformation precursors to the Brumadinho Tailings Dam

724 collapse, Communications Earth & Environment, 2(1), 1-9, 2021.

725 Guthrie, R. H.: Socio-Economic Significance: Canadian Technical Guidelines and Best Practices

726 Related to Landslides: A National Initiative for Loss Reduction, Natural Resources Canada,

727 Ottawa, ON, 2013.

728 Hampel, F. R.: A general qualitative definition of robustness, Ann. Math. Stats., 42(6), 1887-1896,

729 1971.

730 Hongtao, N.: Smart safety early warning model of landslide geological hazard based on BP neural
731 network, Safety Sci., 123, 104572, 2020.

732 Huntley, D., Bobrowsky, P., Charbonneau, F., Journault, J., Macciotta, R., and Hendry, M.:
733 Innovative landslide change detection monitoring: application of space-borne InSAR techniques
734 in the Thompson River valley, British Columbia, Canada, Workshop on World Landslide Forum
735 3, 219-229, 2017.

736 Intrieri, E., Gigli, G., Mugnai, F., Fanti, R., and Casagli, N.: Design and implementation of a
737 landslide early warning system, Eng. Geol., 147, 124-136, 2012.

738 Intrieri, E., Raspini, F., Fumagalli, A., Lu, P., Del Conte, S., Farina, P., Allievi, J., Ferretti, A., and
739 Casagli, N.: The Maoxian landslide as seen from space: detecting precursors of failure with
740 Sentinel-1 data, Landslides, 15(1), 123-133, 2018.

741 Journault, J., Macciotta, R., Hendry, M. T., Charbonneau, F., Huntley, D., and Bobrowsky, P. T.:
742 Measuring displacements of the Thompson River valley landslides, south of Ashcroft, BC,
743 Canada, using satellite InSAR, Landslides, 15(4), 621-636, 2018.

744 Karl, J. H.: Introduction to Digital Signal Processing, Academic Press, San Diego, 1989.

745 Kothari, U.C. and Momayez, M.: New approaches to monitoring, analyzing and predicting slope
746 instabilities, Journal of Geology and Mining Research, 10(1), 1-14, 2018.

747 Lacasse, S., and Nadim, F.: Landslide risk assessment and mitigation strategy, in: Landslides–
748 Disaster Risk Reduction, edited by: Sassa, K., and Canuti, P., Springer, 31-61, 2009.

749 Leroueil, S.: Natural slopes and cuts: movement and failure mechanisms, Géotechnique, 51(3),
750 197-243, 2001.

751 Liu, H., Shah, S., and Jiang, W.: On-line outlier detection and data cleaning, Comput. Chem. Eng.,
752 28(9), 1635-1647, 2004.

753   Macciotta, R., and Hendry, M. T. Remote sensing applications for landslide monitoring and

754   investigation in western Canada, Remote Sens., 13(3), 366-389, 2021.

755   Macciotta, R., Hendry, M., and Martin, C. D.: Developing an early warning system for a very slow

756   landslide based on displacement monitoring, Nat. Hazards, 81(2), 887-907, 2016.

757   Macciotta, R., Carlà, T., Hendry, M., Evans, T., Edwards, T., Farina, P., and Casagli, N.: The 10-

758   mile Slide and response of a retaining wall to its continuous deformation, Workshop on World

759   Landslide Forum, 553-562, 2017a.

760   Macciotta, R., Rodriguez, J., Hendry, M., Martin, C. D., Edwards, T., and Evans, T.: The 10-mile

761   Slide north of Lillooet, British Columbia–history, characteristics, and monitoring. In Proceedings,

762   3rd North American Symposium on Landslides, 937-948, 2017b.

763   Pearson, R. K.: Outliers in process modeling and identification, IEEE Trans. Control Syst.

764   Technol., 10(1), 55-63, 2002.

765   Reid, M. E., Godt, J. W., LaHusen, R. G., Slaughter, S. L., Badger, T. C., Collins, B. D., Schulz,

766   W. H., Baum, R. L., Coe, J. A., Harp, E. L. and Schmidt, K. M.: When hazard avoidance is not an

767   option: lessons learned from monitoring the postdisaster Oso landslide, USA, Landslides, 18,

768   2993-3009, 2021.

769   Rodriguez, J. L., Macciotta, R., Hendry, M., Edwards, T., and Evans, T.: Slope hazards and risk

770   engineering in the Canadian railway network through the Cordillera, Proceedings of the AIIT

771   International Congress on Transport Infrastructure and Systems (TIS 2017), Rome, Italy, 163-

772   168, 2017.

773   Rodriguez, J., Hendry, M., Macciotta, R., and Evans, T.: Cost-effective landslide monitoring GPS

774   system: characteristics, implementation, and results, Geohazards7, Canmore, Alberta, 2018.

775 Rodriguez, J., Macciotta, R., Hendry, M. T., Roustaei, M., Gräpel, C., and Skirrow, R.: UAVs for

776 monitoring, investigation, and mitigation design of a rock slope with multiple failure mechanisms—

777 a case study, Landslides, 17, 2027-2040, 2020.

778 Rousseeuw, P. J., and Hubert, M.: Robust statistics for outlier detection. Wiley Interdiscip. Rev.

779 Data Min. Knowl. Discov., 1(1), 73-79, 2011.

780 Salgado, C. M., Azevodo, C., Proença, H., and Vieira, S. M.: Noise versus outliers. In: Secondary

781 Analysis of Electronic Health Records, MIT Critical Data, Springer, 163-183, 2016.

782 Savitzky, A., and Golay, M. J.: Smoothing and differentiation of data by simplified least squares

783 procedures, Anal. Chem., 36(8), 1627-1639, 1964.

784 Schafer, M. B.: Kinematics and Controlling Mechanics of Slow-moving Ripley Landslide.

785 Dissertation, University of Alberta, 2016.

786 Schafer, R. W.: What is a Savitzky-Golay filter? [lecture notes], IEEE Signal Process. Mag., 28(4),

787 111-117, 2011.

788 Scoppettuolo, M.R., Cascini, L., and Babilio, E.: Typical displacement behaviours of slope

789 movements, Landslides, 17, 1105-1116. 2020

790 Smith, S.: Digital Signal Processing: A Practical Guide for Engineers and Scientists, Elsevier,

791 2013.

792 Thiebes, B., Bell, R., Glade, T., Jäger, S., Mayer, J., Anderson, M., and Holcombe, L.: Integration

793 of a limit-equilibrium model into a landslide early warning system, Landslides, 11(5), 859-875,

794 2014.

795 Tofani, V., Rasipini, F., Catani, F., and Casagli, N.: Persistent Scatterer Interferometry (PSI)

796 technique for landslide characterization and monitoring, Remote Sens., 5(3), 1045-1065, 2013.

UNISDR: United Nations International Strategy for Disaster Reduction: Terminology on Disaster Risk Reduction, 2009. Available at http://www.unisdr.org.

Vaziri, A., Moore, L., and Ali, H.: Monitoring systems for warning impending failures in slopes and open pit mines, Nat. Hazards, 55(2), 501-512, 2010.

Wang, G.: GPS landslide monitoring: single base vs. network solutions-a case study based on the Puerto Rico and Virgin Islands permanent GPS network, J. Geodet. Sci., 1(3), 191-203, 2011.

William, S. C.: Robust locally weighted regression and smoothing scatterplots. J. Am. Stat. Assoc., 74(368), 829-836, 1979.

Woods, A., Hendry, M. T., Macciotta, R., Stewart, T., and Marsh, J.: GB-InSAR monitoring of vegetated and snow-covered slopes in remote mountainous environments, Landslides, 17, 1713-1726, 2020.

Woods, A., Macciotta, R., Hendry, M. T., Stewart, T., and Marsh, J.: Updated understanding of the deformation characteristics of the Checkerboard Creek rock slope through GB-InSAR monitoring, Eng. Geol., 281, 105974, 2021.

Yao, Z., Xie, J., Tian, Y., and Huang, Q.: Using Hampel identifier to eliminate profile-isolated outliers in laser vision measurement, J. Sens., 2019, 3823691, 2019.

Yin, Y., Wang, H., Gao, Y., and Li, X.: Real-time monitoring and early warning of landslides at relocated Wushan Tow, the Three Gorges Reservoir, China, Landslides, 7(3), 339-349, 2010.

Zhang, Y.H., Ma, H.T. and Yu, Z.X.: Application of the method for prediction of the failure location and time based on monitoring of a slope using synthetic aperture radar, Environ. Earth Sci., 80(21) 1-13, 2021a.

Zhang, Y. G., Tang, J., He, Z. Y., Tan, J., and Li, C.: A novel displacement prediction method using gated recurrent unit model with time series analysis in the Erdaohe landslide. Nat. Hazards, 105, 783-813, 2021b.

821   Zhou, X.P., Liu, L.J., and Xu, C.: A modified inverse-velocity method for predicting the failure time

822   of landslides, Eng. Geol., 268, 105521, 2020.

823   Zimek, A., and Filzmoser, P.: There and back again: Outlier detection between statistical

824   reasoning and data mining algorithms, Data Min. Knowl. Discov., 8(6), 1280, 2018.

825